

A UNIVERSAL DECLINE LAW OF CLASSICAL NOVAE. III. GQ MUS 1983

IZUMI HACHISU

Department of Earth Science and Astronomy, College of Arts and Sciences, University of Tokyo, Komaba, Meguro-ku, Tokyo 153-8902, Japan

MARIKO KATO

Department of Astronomy, Keio University, Hiyoshi, Kouhoku-ku, Yokohama 223-8521, Japan

AND

ANGELO CASSATELLA

INAF, Istituto di Fisica dello Spazio Interplanetario, Via del Fosso del Cavaliere 100, 00133 Rome, Italy

to appear in the *Astrophysical Journal*

ABSTRACT

We present a unified model of infrared (IR), optical, ultraviolet (UV), and X-ray light curves for the 1983 outburst of GQ Muscae (Nova Muscae 1983) and estimate its white dwarf (WD) mass. Based on an optically thick wind model of nova outbursts, we model the optical and IR light curves with free-free emission, and the UV 1455 Å and supersoft X-ray light curves with blackbody emission. The best fit model that reproduces simultaneously the IR, optical, UV 1455 Å, and supersoft X-ray observations is a $0.7 \pm 0.05 M_{\odot}$ WD for an assumed chemical composition of the envelope, $X = 0.35 - 0.55$, $X_{\text{CNO}} = 0.2 - 0.35$, and $Z = 0.02$, by mass weight. The mass lost by the wind is estimated to be $\Delta M_{\text{wind}} \sim 2 \times 10^{-5} M_{\odot}$. We provide a new determination of the reddening, $E(B - V) = 0.55 \pm 0.05$, and of the distance, ~ 5 kpc. Finally, we discuss the strong UV flash that took place on JD 2,445,499 (151 days after the outburst).

Subject headings: novae, cataclysmic variables — stars: individual (GQ Muscae) — stars: mass loss — ultraviolet: stars — white dwarfs — X-rays: binaries

1. INTRODUCTION

Despite their overall similarity, the optical light curves of classical novae show a wide variety of timescales and shapes (e.g., Payne-Gaposchkin 1957). Various empirical time-scaling laws have been proposed in the attempt to recognize common patterns and to unify the nova light curves. For example, McLaughlin (1942) proposed a compression of the time scale obtained by normalizing the time to t_m , the time for the brightness to decrease by m magnitudes (usually $m = 2$ or 3). The results were however unsatisfactory because slow novae reached their late stages relatively earlier than faster novae. A different approach was adopted by Vorontsov-Velyaminov (1948) who, based on a large collection of nova light curves, found that $m(t)$, the visual magnitude at time t , is conveniently represented, on average, by $m(t) = m_0 + b_1 \log(t - t_0)$ at early stages and $m(t) = m_1 + b_2 \log(t - t_0)$ at later stages with $b_1 = 2.5$ and $b_2 > b_1$.

The underlying problem of both the above approaches is that, during the decline phase from maximum, the flux in the visual band, initially dominated by free-free emission, becomes more and more affected by the increasing contribution from the emission lines, which finally dominates. The presence of these two competing and heterogeneous emission mechanisms is most likely the main cause for the difficulty to find a suitable normalization parameter for the nova light curves. A more appropriate way to monitor the evolution of the visual continuum is to use the Strömgren y filter, which is designed to avoid strong emission lines and, in particular, the [O III] line (e.g., Kaler 1986; Lockwood & Millis 1976). In the case of V1668 Cyg, Kaler (1986) has indeed shown that

the continuum y flux declines much faster than the H β +[O III] fluxes. Consequently, the decline rate is much faster in the y band than in the visual band. This was demonstrated by Kaler (1986), who showed that the y magnitude of V1668 Cyg declines with a slope of $b_1 = 3.5$ at early stages and it then changes to $b_2 = 6.5$ at later stages, values that are sensibly larger than those reported by Vorontsov-Velyaminov (1948).

The observations of V1500 Cyg by Gallagher & Ney (1976) suggest that the visual and infrared continua are well represented by free-free emission during the early decay phase. The same applies to GQ Mus: Krautter et al. (1984) reported that, during the early 40 days (diffuse enhanced and Orion-phases), the energy spectrum of $0.3 - 10 \mu$ was well represented by optically thin free-free emission (see also Dinerstein 1986). The flux in the optical and infrared appears to decay with time as $F_{\lambda} \propto t^{-\alpha}$ in various speed classes of novae (e.g., Ennis et al. 1977; Woodward et al. 1997, for V1500 Cyg).

An interesting attempt to unify the light curves of novae was proposed by Rosenbush (1999a,b), who suggested that the main parameter determining the shape of the light curve is the radius of the ejected shell, $\log R_{\text{shell}} = \log(t) + \log(v)$, where t is the time from optical maximum, and v is the velocity of the ejecta. He plotted various nova light curves in the $m - \log R_{\text{shell}}$ diagram and found that light curves overlapped each other. The rather large scatter of the data in that diagram is probably due to the fact that the expansion velocity of novae varies with time (see Cassatella et al. 2005).

Cassatella et al. (2002) studied the time evolution of the UV continuum flux in twelve CO and ONeMg novae and found a strong correlation between the t_3 time and the time of maximum flux in the 1455 Å continuum (see Fig. 4 in their paper). In a subsequent paper, Cassatella et al. (2005) stud-

Electronic address: hachisu@ea.c.u-tokyo.ac.jp
Electronic address: mariko@educ.cc.keio.ac.jp
Electronic address: cassatella@fis.uniroma3.it

ied the time evolution of the UV emission lines in seven CO novae and found a strong correlation between the line ionization potential and the time of maximum emission normalized to the t_3 (Fig. 5 in their paper). These results strongly suggest that novae do indeed evolve following a common pattern being time-normalized by the t_3 time, which mainly depends on the white dwarf mass (e.g., Livio 1992).

Recently, Hachisu & Kato (2006, hereafter referred as Paper I) found that the visual and IR light curves of several novae follow a universal decline law, and interpreted that in terms of free-free emission (Paper I; Hachisu & Kato 2007, hereafter referred as Paper II); in particular, the time-normalized light curves were found to be independent of the white dwarf mass, the chemical composition of ejecta, and wavelength. They also showed that the UV 1455 Å light curve, interpreted as blackbody continuum, can also be time-normalized by the same factor as in the optical and IR. The authors, in the above quoted papers, determined the white dwarf mass and other parameters for a number of relatively well-observed classical novae.

In the present paper, we apply the above universal decline law to the classical nova GQ Muscae 1983. GQ Mus is the first classical nova in which the supersoft X-ray turnoff was detected with the X-ray satellite *ROSAT* (Ögelman et al. 1993; Balman et al. 1998; Orío et al. 2001). This object was also well observed by the UV satellite *IUE* (e.g., Krautter et al. 1984) and in near-IR bands of *JHKL* (e.g., Whitelock et al. 1984).

The next section summarizes the basic observational characteristics of GQ Mus. In §3, we revisit the UV light curves of GQ Mus obtained with the *IUE* satellite. In §4, we briefly introduce our method based on our optically thick wind model. Light curve fittings of GQ Mus in the X-ray, UV, optical, and near IR bands are shown in §5. Discussion and conclusions follow in §§6 and 7, respectively. Finally, in the Appendix, we assess the problem of the contribution of the emission lines to the visual and infrared photometric bands for GQ Mus and for other well known novae: V1500 Cyg, V1668 Cyg, and V1974 Cyg.

2. BASIC OBSERVATIONAL SUMMARY OF GQ MUSCAE 1983

GQ Mus was discovered by Liller on 1983 January 18.14 UT (JD 2,445,352.64) at $m_V \approx 7.2$ (Liller & Overbeek 1983). Bateson (1983) reported two pre-discovery magnitudes, i.e., $m_V \approx 7.6$ obtained by Gainsford on 1983 January 15.597 UT (2,445,350.097) and $m_V \approx 7.9$ obtained by Pattie on 1983 January 15.628 UT (2,445,350.128). Krautter et al. (1984) suggested that the outburst took place 3–4 days before the discovery. In absence of precise estimates, we assume that the outburst took place at $t_{OB} = \text{JD } 2,445,348.0$ (1983 January 13.5 UT), i.e., 4.6 days before the discovery by Liller on January 18.14, and adopt $t_{OB} = \text{JD } 2,445,348.0$ as day zero in the following analysis.

Early optical *UBVRI* and near infrared *JHKL* observations of GQ Mus show a fast evolution with $t_2 \sim 18$ days and $t_3 = 48$ days (Whitelock et al. 1984). Krautter et al. (1984) observed GQ Mus over a wide wavelength range from 0.12 – 10 μ during the early 40 days (diffuse enhanced and Orion-phases). These authors reported an extraordinary large amplitude brightening by $\Delta m_V \sim 14$ mag, with respect to the prenova magnitude of $m_V \gtrsim 21$. After about 4 months of slow decline, the brightness stabilized in the range $m_V \sim 10$ –11 for about 400 days. After that, the nova gradually declined to $m_V \sim 14$ for another 400 days (see figures below).

In this paper we will use the optical and IR photometric data from Whitelock et al. (1984) and Krautter et al. (1984), which cover about 300 days after discovery. No other systematic photometric observations are available at later stages except for the visual magnitude measurements (V_{FES}) obtained with the Fine Error Sensor (FES) monitor on board *IUE*, which cover 500 days after discovery, and the visual photometric data collected by RASNZ (Royal Astronomical Society of New Zealand) and by AAVSO (American Association of Variable Star Observers), which cover 1000 days after discovery.

Diaz & Steiner (1989) determined a photometric orbital period of 0.0594 days for GQ Mus, the shortest known for a classical nova. Later on, Diaz & Steiner (1994) revised the ephemeris of GQ Mus based on the 1989 and 1990 photometric observations, i.e.,

$$\text{HJD}_{\min} = 2,447,843.4721 + 0.0593650 \times E. \quad (1)$$

We have adopted this ephemeris for our binary model. Diaz & Steiner (1989, 1994) also suggested that GQ Mus is a polar system because of the presence of X-ray emission and high (He II $\lambda 4686$)/ $H\beta$ ratio.

Based on the optical observation from 1984 March to 1988 March (400 – 1800 days after the outburst), Krautter & Williams (1989) suggested that the observed progressive increase in the ionization level of the nova shell was due to a very hot radiation source with a temperature of $> 4 \times 10^5$ K, increasing with time while the bolometric luminosity remained constant. Ögelman et al. (1987) studied the soft X-ray *EXOSAT* light curve from optical maximum to about 900 days after it, and suggested a model of a very hot white dwarf remnant with a maximum temperature of $(2-4) \times 10^5$ K evolving at constant bolometric luminosity.

ROSAT observations clearly show that the supersoft X-ray flux decayed about 10 yr after the outburst (Ögelman et al. 1993; Shanley et al. 1995; Orío et al. 2001; Balman & Krautter 2001). This information is very important because, compared with our model predictions, it allows one to determine the white dwarf mass quite accurately (see, e.g., Paper I).

3. UV OBSERVATIONS

One of the most puzzling features of GQ Mus is its long lasting brightness in the UV range, which made possible its regular monitoring by *IUE* over as much as 11.5 yr. Because of satellite constraints, the *IUE* observations could not start before JD 2,445,385.07, i.e., 32.4 days after discovery. The early *IUE* observations of GQ Mus are discussed in detail by Krautter et al. (1984). In the following we revisit the problem of the color excess $E(B-V)$ of GQ Mus and describe the long term evolution of the ultraviolet continuum and of the emission lines, as well as the secondary outburst which took place about 151 days after the main one. The ultraviolet spectra were retrieved from the *IUE* archive through the INES (*IUE* Newly Extracted Spectra) system¹, which also provides details of the observations. The use of *IUE* INES data is particularly important for the determination of the reddening correction because of the implementation of upgraded spectral extraction and flux calibration procedures compared to previously published UV spectra.

¹ <http://ines.laeff.esa.es>

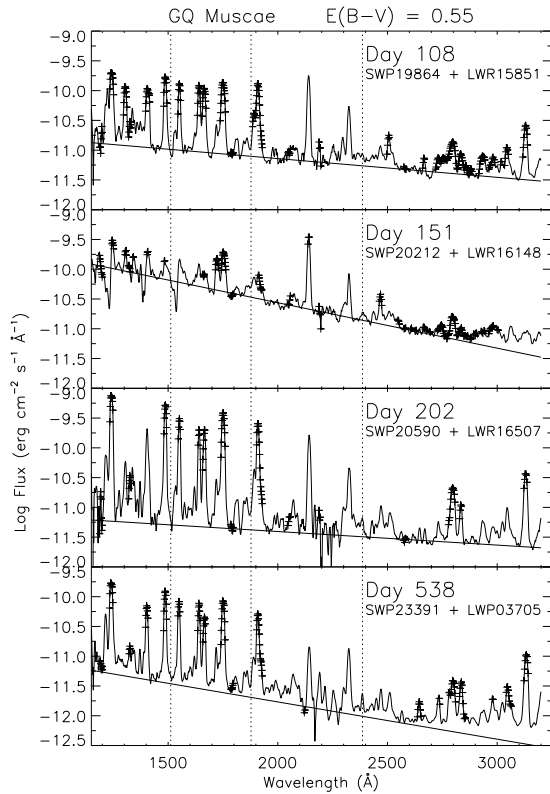


FIG. 1.— *IUE* spectra of GQ Mus obtained at four epochs, i.e., 108, 151, 202, and 538 days after the outburst. The spectra have been corrected for reddening using $E(B-V) = 0.55$. The vertical dotted lines represent the wavelengths $\lambda\lambda$ 1512, 1878 and 2386 Å at which the extinction law takes the same value. With the adopted value of reddening, the stellar continuum underlying the many emission lines is well represented by a straight line all over the full spectral range except for the spectrum of day 538 above 2700 Å, due to the increased contribution from hydrogen Balmer continuum. Saturated points in the emission lines are denoted by pluses. Note the comparably harder spectrum at the time of the secondary outburst on day 151.

3.1. The reddening correction

The color excess of GQ Mus has been determined from the hydrogen Balmer lines by de Freitas Pacheco & Codina (1985) and Péquignot et al. (1993), who found $E(B-V) = 0.43$ and 0.50 ± 0.05 , respectively. About the same range of values has been reported by Krautter et al. (1984) and Hassall et al. (1990), who found $E(B-V) = 0.45$ and 0.50 , respectively, based on the strength of the dust absorption band around 2175 Å in the early *IUE* spectra. Given the criticality of the reddening correction, we have attempted to improve its accuracy by using two independent methods based on the shape of the UV continuum and on the emission line intensities.

The Galactic extinction curve (Seaton 1979) shows a pronounced broad maximum around 2175 Å due to dust absorption, but it takes the same value $X(\lambda) = A(\lambda)/E(B-V) \approx 8$ at $\lambda = 1512, 1878, \text{ and } 2386$ Å, so that the slope of the straight line passing through the continuum points at these wavelengths is insensitive to $E(B-V)$ in a $(\lambda, \log F(\lambda))$ plot. This circumstance can be used to get a reliable estimate of $E(B-V)$ as that in which the stellar continuum becomes closely linear in the 1512–2386 Å region, and passes through the continuum points at the above wavelengths. From 8 pairs of short and long wavelength *IUE* spectra taken during the nebular phase we have in this way found $E(B-V) = 0.58 \pm 0.04$.

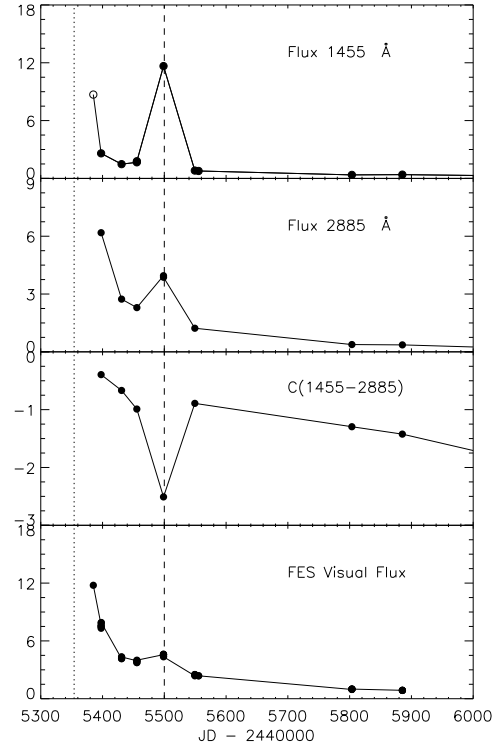


FIG. 2.— Time evolution of the continuum fluxes at 1455 Å and 2885 Å, of the ultraviolet color index $C(1455-2885)$, and of the visual flux. Fluxes are in units of 10^{-13} erg cm^{-2} s^{-1} Å^{-1} , not corrected for reddening. Only the color index has been corrected for reddening using $E(B-V) = 0.55$. The vertical dotted and dashed lines indicate the date of discovery and that of the secondary outburst, respectively.

A different way to estimate the $E(B-V)$ color excess consists in using the observed relative intensities of the He II 1640 Å Balmer line, and the 2734 and 3203 Å Paschen recombination lines, and compare these with theoretical ratios (Hummer & Storey 1987). The intensity ratios $I(1640)/I(2734)$ and $I(1640)/I(3203)$ were measured in 8 pairs of short and long wavelength *IUE* low resolution spectra obtained during the nebular phase. From a comparison with the theoretical values for an electron temperature and density of $(T_e, N_e) = (20,000 \text{ K}, 10^6 \text{ cm}^{-3})$ we have obtained 22 independent determinations of the color excess leading to a mean value of $E(B-V) = 0.51 \pm 0.06$. In the following we will adopt the error-weighted mean of the two above determinations, i.e. $E(B-V) = 0.55 \pm 0.05$. Examples of *IUE* spectra of GQ Mus corrected with $E(B-V) = 0.55$ are reported in Figure 1 for the following days (after the outburst): 108, 151 (secondary outburst; see later), 202 and 538.

3.2. Evolution of the UV continuum

We have measured the mean flux in two narrow bands 20 Å wide centered at 1455 Å and 2855 Å, selected to best represent the UV continuum because little affected by emission lines (Cassatella et al. 2002). Figure 2 shows the time evolution of the $F(1455 \text{ Å})$ and $F(2885 \text{ Å})$ fluxes and of the UV color index $C(1455-2885) = -2.5 \log[F(1455 \text{ Å})/F(2885 \text{ Å})]$. The measurements were made on well exposed low resolution large aperture spectra. Unfortunately, the *IUE* spectrum of day 37 (SWP19299), very important because it was the first obtained, was heavily satu-

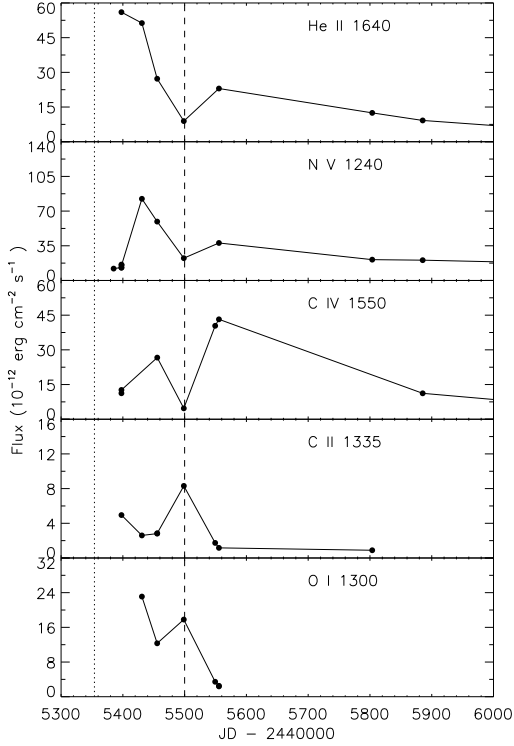


FIG. 3.— Time evolution of the observed fluxes in the most prominent permitted emission lines of GQ Mus, in units of 10^{-12} erg cm^{-2} s^{-1} . The vertical dotted and dashed lines indicate the date of discovery and that of the secondary outburst, respectively.

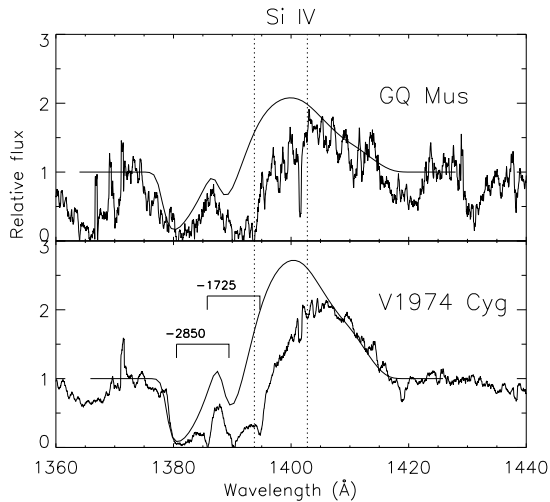


FIG. 4.— The figure shows the P Cygni profile of the Si IV doublet $\lambda\lambda$ 1393.74, 1402.77 Å of GQ Mus at the time of the secondary outburst on day 150.64 (upper panel) and, for comparison, that of the Neon nova V1974 Cyg obtained on day 45 after discovery (lower panel): the *IUE* images used are SWP 20211 and SWP44390, respectively. The observed profiles have been fitted with theoretical P Cygni profiles obtained through the SEI method (Lamers et al. 1987; Groenewegen & Lamers 1989). Fluxes are normalized to the local continuum. The wind terminal velocity derived from the observed profiles is 3200 km s^{-1} in both cases. The laboratory wavelengths of the doublet are indicated as vertical dotted lines. The figure indicates also the position of the violet shifted absorption components from the principal system at 1725 and 2850 km s^{-1} in V 1974 Cygni (Cassatella et al. 2004). Such components cannot be clearly distinguished in GQ Mus due to the poor signal quality (the spectrum is the result of a 11-point running smoothing average).

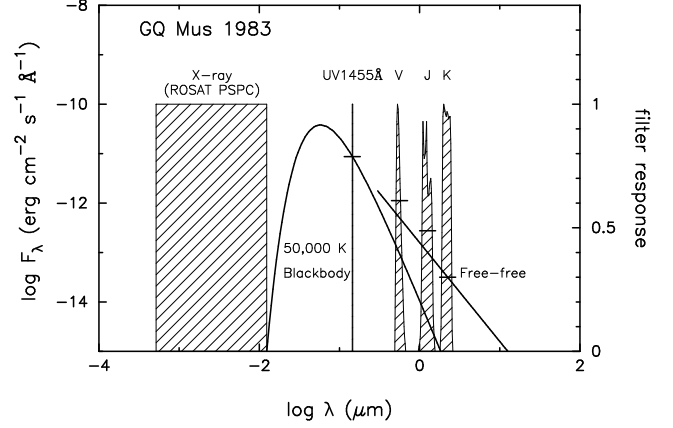


FIG. 5.— Schematic representation of the energy spectrum of GQ Mus according to our model. The passbands of the photometric filters used in this work is indicated. The UV 1455 Å and supersoft X-ray (0.1–2.4 keV) fluxes are calculated from a blackbody spectrum, while the *V*, *J*, *H*, and *K* magnitudes are from a free-free emission spectrum as shown in the figure. Note that the flux scale of the dereddened blackbody and of the free-free emission corresponds to our $0.7 M_{\odot}$ white dwarf model on day 180 as shown in Fig. 7, assuming a reddening of $E(B-V) = 0.55$. Horizontal short lines denote the energy flux in each filter on day 180; some of them are interpolated from other observational points. The soft X-ray flux is negligibly small on that day. The *V* and *J* magnitudes are larger than those of free-free because these bands are heavily contaminated by strong emission lines as explained in the Appendix.

rated around 1455 Å. To make a crude estimate of the corresponding flux we have determined the scaling factor between this and the next spectrum obtained on day 49 (SWP 19383), in a region where both were well exposed (1520–1620 Å), and assumed that the spectral slope remained the same in the two spectra. The value so obtained, reported as an open circle in Figure 2, likely represents an upper limit to the true value because, as shown in the same figure, the UV color was comparatively cooler in the first observations. Figure 2 reports also, for comparison, the visual light curve obtained from the Fine Error Sensor (FES) counts on board *IUE*, once corrected for FES time dependent sensitivity degradation (see Cassatella et al. 2004 for details on the FES calibration).

It appears from Figure 2 that the gradual fading of the UV and visual fluxes was interrupted, around JD 2,445,499 (day 151), by a secondary outburst, as also noticed by Hassall et al. (1990). The secondary outburst had actually the appearance of a “UV flash” because of its especially large amplitude at short wavelengths. Indeed, compared with the *IUE* low resolution observations obtained just before and after this event (days 108 and 202), the UV flux increased by a factor of 9 at 1455 Å and by a factor 2.2 at 2885 Å, while the visual flux increased only by a factor of 1.5. The consequent hardening of the UV continuum is also reflected by the upturn of the $C(1455-2885)$ color index, as shown in the same figure.

3.3. Evolution of the UV emission lines

Also the UV emission lines suffered from important changes in coincidence with the secondary outburst of day 151, as shown in Figure 3, which reports, as a function of time, the flux in the most prominent permitted UV emission lines, as measured by us from the available *IUE* low resolution spectra. The figure shows that, on day 151, the flux of the high ionization emission lines (He II 1640 Å, N V 1240 Å and C IV 1550 Å) had decreased substantially while, on the contrary, it increased in the low ionization resonance lines of

TABLE 1
CHEMICAL ABUNDANCE BY WEIGHT

object	H	CNO	Ne	Na-Fe	reference
Solar composition	0.7068	0.0140	0.0018	0.0034	Grevesse & Anders (1989)
GQ Mus 1983	0.37	0.24	0.0023	0.0039	Morisset & Péquignot (1996a)
GQ Mus 1983	0.27	0.40	0.0034	0.023	Hassall et al. (1990)
GQ Mus 1983	0.43	0.19	Andreae & Drechsel (1990)

C II and O I, so implying a drastic change of the ionization structure of the emitting regions.

The other important feature of the secondary outburst was the appearance of a strong P Cygni profile in the Si IV doublet $\lambda\lambda$ 1393.74, 1402.77 Å, shown in Figure 4. The figure reports also, for comparison, the Si IV profile of the Neon Nova V1974 Cyg obtained 45 days after the outburst. A comparison of observed with theoretical P Cygni profiles computed with the SEI method (Lamers et al. 1987; Groenewegen & Lamers 1989) indicate that the terminal velocity of the wind was about the same for the two novae ($\approx 3200 \text{ km s}^{-1}$). The special interest of the observations in Figure 4 is that GQ Mus had entered the nebular phase well before day 151, so that the presence of P Cygni profiles was not expected to be detectable at this stage. Indeed, P Cygni profiles were not detectable in an earlier *IUE* high resolution spectrum of day 49, despite the factor of two longer exposure time, nor they were at later stages. This strongly suggests that a short duration mass ejection episode took place around day 151. This episode caused efficient recombination to take place in the emitting region, observed as a substantial, although transitory, fainting of the high ionization emission lines (cf. Fig.3). The fast recovery of the emission line spectrum by day 202 suggests that the ejected mass must have been small. Also the presence of a flare at UV wavelengths rather than in the optical (cf. Fig. 2) requires a small opacity in the UV and then a small ejected mass.

4. MODELING OF NOVA OUTBURSTS

We present a unified model for the IR, optical, UV, and supersoft X-ray light curves of the 1983 outburst of GQ Mus. As in Paper I, our models are based on the optically thick wind theory of nova outbursts described in Kato & Hachisu (1994).

4.1. Optically thick wind model

After a thermonuclear runaway sets in on a mass-accreting WD, its envelope expands greatly to $R_{\text{ph}} \gtrsim 100 R_{\odot}$, where R_{ph} is the photospheric radius, and it then settles onto steady-state regime. The decay phase of the nova can be followed by a sequence of steady state solutions (e.g., Kato & Hachisu 1994). Using the same method and numerical techniques as in Kato & Hachisu (1994), we have followed the nova evolution by connecting steady state solutions along the envelope mass-decreasing sequence.

The equations of motion, radiative diffusion, and conservation of energy are solved from the bottom of the hydrogen-rich envelope through the photosphere under the condition that the solution goes through a critical point of a steady-state wind. The winds are accelerated deep inside the photosphere so that they are called “optically thick winds.” We have used updated OPAL opacities (Iglesias & Rogers 1996). One of the boundary conditions for our numerical code consists in assuming that photons are emitted at the photosphere as a blackbody with a photospheric temperature T_{ph} . X-ray and UV fluxes are

estimated directly from the blackbody emission, but infrared and optical fluxes are calculated from free-free emission by using physical values of our wind solutions as mentioned below in §4.3. Physical properties of these wind solutions have already been published (e.g., Hachisu & Kato 2001a,b, 2004; Hachisu et al. 1996, 1999a,b, 2000, 2003; Kato 1983, 1997, 1999).

Optically thick winds stop after a large part of the envelope is blown in the winds. The envelope settles into hydrostatic equilibrium, while its mass decreases in time by nuclear burning. Then we solve the equation of static balance instead of the equation of motion. When the nuclear burning decays, the WD enters a cooling phase, in which the luminosity is supplied with heat flow from the ash of hydrogen burning.

4.2. Multiwavelength light curves

In the optically thick wind model, a large part of the envelope is ejected continuously during a relatively long period (e.g., Kato & Hachisu 1994). After maximum expansion, the photospheric radius gradually decreases keeping the total luminosity (L_{ph}) almost constant. The photospheric temperature (T_{ph}) increases with time because of $L_{\text{ph}} = 4\pi R_{\text{ph}}^2 \sigma T_{\text{ph}}^4$. The maximum emission shifts from the optical to supersoft X-ray through ultraviolet (UV) and extreme ultraviolet (EUV). This causes the luminosity to decrease in the optical and to increase in the UV, until it reaches a maximum. The following decay in the UV is accompanied by an increase of the supersoft X-ray range. These timescales depend crucially on the WD parameters such as the WD mass and the chemical composition of the envelope (e.g. Kato 1997, Paper I). Thus, we can follow the development of optical, UV, and supersoft X-ray light curves by a single modeled sequence of steady wind solutions.

4.3. Free-free light curves

Spectra of novae show blackbody features at very early stages, but free-free emission from optically thin plasma will eventually dominate (e.g., Gallagher & Ney 1976; Krautter et al. 1984). During the optically thick wind phase (see Paper I for more details), the extended regions outside the photosphere are optically thin. The optical and IR free-free emission fluxes arising from these regions can be estimated from

$$F_{\nu} \propto \int N_e N_i dV \propto \int_{R_{\text{ph}}}^{\infty} \frac{\dot{M}_{\text{wind}}^2}{v_{\text{wind}}^2 r^4} r^2 dr \propto \frac{\dot{M}_{\text{wind}}^2}{v_{\text{ph}}^2 R_{\text{ph}}}, \quad (2)$$

where F_{ν} is the flux at the frequency ν , N_e and N_i are the number densities of electrons and ions, respectively, V is the volume of the optically thin region, R_{ph} is the photospheric radius, \dot{M}_{wind} is the wind mass loss rate, and v_{ph} is the photospheric velocity. In equation (2) we assume that the electron temperature and the degree of ionization are constant in the free-free emitting region. We also assume that $N_e \propto \rho_{\text{wind}}$, $N_i \propto \rho_{\text{wind}}$, and use the continuity equation, i.e.,

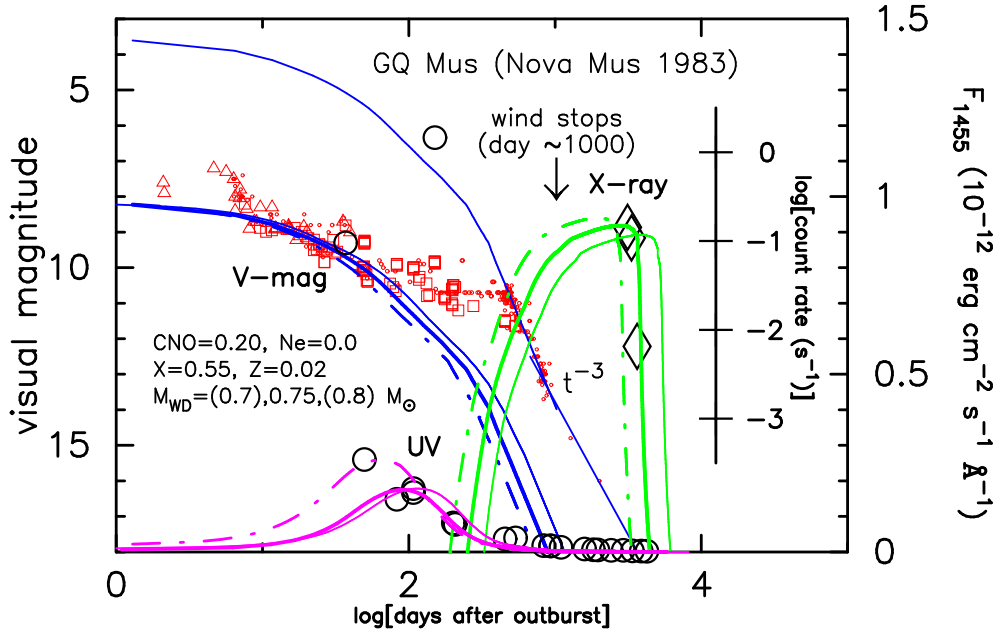


FIG. 6.— Calculated light curves of free-free V magnitude, UV 1455 Å, and supersoft X-ray (0.1–2.4 keV) fluxes are compared with the observations. *Open diamonds*: *ROSAT* X-ray (0.1–2.4 keV) observations from Shanley et al. (1995) and Origo et al. (2001). *Open circles*: *IUE* UV 1455 Å observations. *Open triangles*: visual and V magnitudes are from IAU Circulars 3764, 3766, 3771, 3782, and 3853. *Open squares*: V magnitude observations from Whitelock et al. (1984) and *IUE* V_{FES} data. *Small circles*: visual magnitude observations from RASNZ and AAVSO. Our best-fit model consists of the white dwarf with mass $0.75 M_{\odot}$ for the envelope chemical composition of $X = 0.55$, $X_{\text{CNO}} = 0.20$, and $Z = 0.02$. An arrow indicates the epoch when the optically thick wind stops. The upper thin solid line is the same as the thick solid line, but lifted up by 4.5 mag to represent contribution of strong emission lines to the V bandpass (Papers I and II). Model predictions for white dwarf masses $M_{\text{WD}} = 0.7 M_{\odot}$ (thin solid line) and $M_{\text{WD}} = 0.8 M_{\odot}$ (dash-dotted line) are also added for comparison.

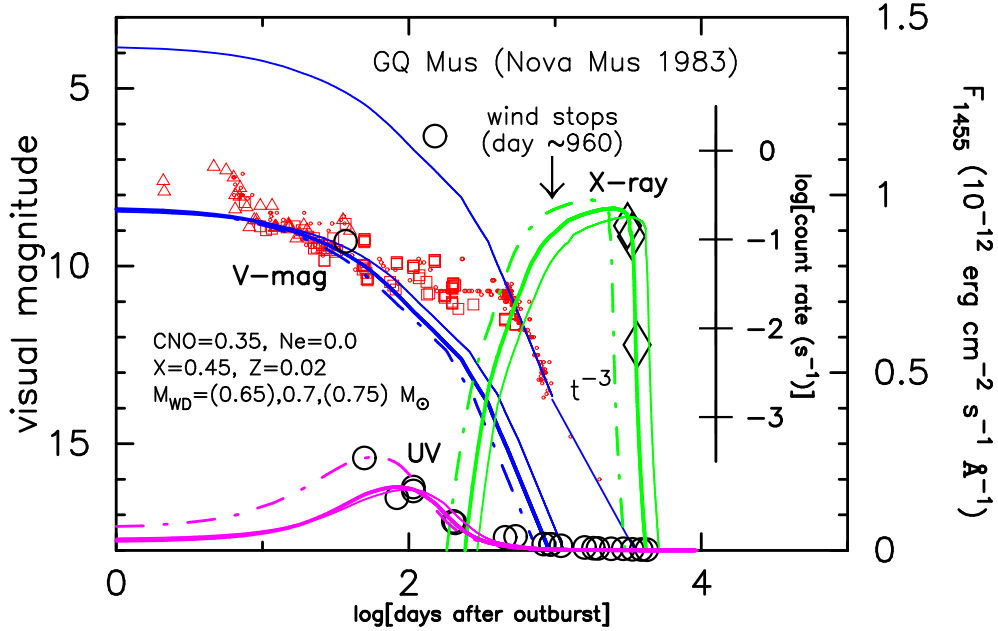


FIG. 7.— Same as in Fig. 6, but for our best-fit model of $M_{\text{WD}} = 0.7 M_{\odot}$ for the envelope chemical composition of $X = 0.45$, $X_{\text{CNO}} = 0.35$, and $Z = 0.02$. Two other cases of the white dwarf mass, $M_{\text{WD}} = 0.65 M_{\odot}$ (thin solid line) and $M_{\text{WD}} = 0.75 M_{\odot}$ (dash-dotted line) are also added for comparison.

$\rho_{\text{wind}} = \dot{M}_{\text{wind}} / 4\pi r^2 v_{\text{wind}}$, where ρ_{wind} and v_{wind} are the density and velocity of the wind, respectively. Finally, we assume that $v_{\text{wind}} = \text{const.} = v_{\text{ph}}$ in the optically thin region.

After the optically thick wind stops, the total mass of the ejecta remains constant in time. The flux from such homolo-

gously expanding ejecta is approximately given by

$$F_{\nu} \propto \int N_e N_i dV \propto \rho_{\text{ej}}^2 V_{\text{ej}} \propto \left(\frac{M_{\text{ej}}}{V_{\text{ej}}} \right)^2 V_{\text{ej}} \propto V_{\text{ej}}^{-1} \propto R^{-3} \propto t^{-3}, \quad (3)$$

where ρ_{ej} , V_{ej} , and $M_{\text{ej}} (= \text{const.})$ are the density, volume, and total mass, respectively, of the ejecta. We assume that the ejecta are expanding at a constant velocity, v . So we have the radius of the ejecta of $R = vt$, where t is the time after the

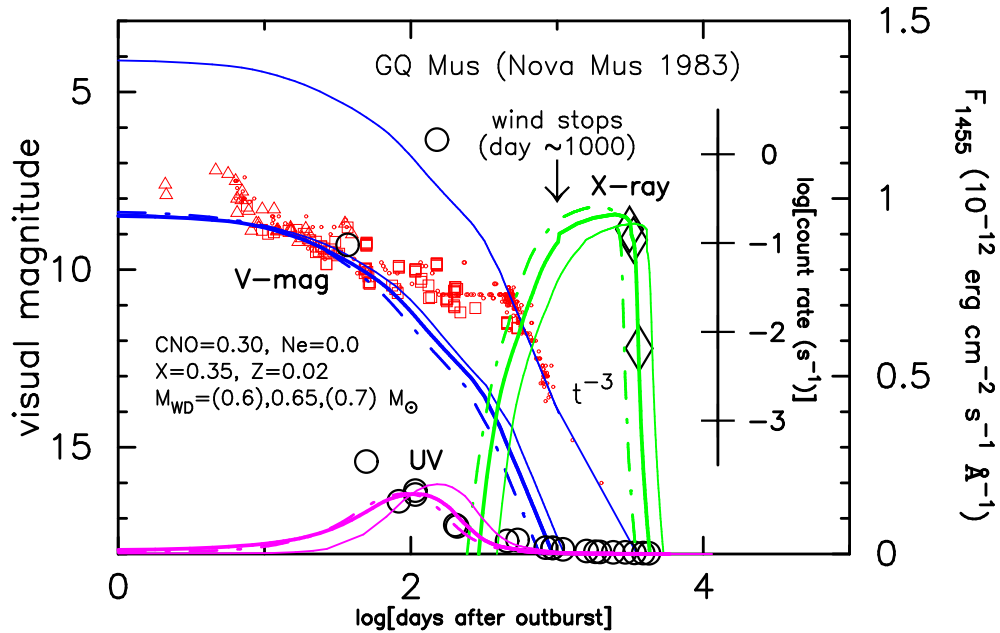


FIG. 8.— Same as Fig. 6, but for our best-fit model of the white dwarf mass of $0.65 M_{\odot}$ for the envelope chemical composition of $X = 0.35$, $X_{\text{CNO}} = 0.30$, and $Z = 0.02$. Two other cases of the white dwarf mass, $M_{\text{WD}} = 0.6 M_{\odot}$ (thin solid line) and $M_{\text{WD}} = 0.7 M_{\odot}$ (dash-dotted line) are also added for comparison.

outburst. The proportionality constants in equations (2) and (3) cannot be determined a priori because radiative transfer is not calculated outside the photosphere: these were determined using the procedure described below in §5.

4.4. System parameters of optically thick wind model

The light curves of our optically thick wind model are parameterized by the WD mass (M_{WD}), the chemical composition of the envelope (X , X_{CNO} , X_{Ne} , and Z), and the envelope mass ($\Delta M_{\text{env},0}$) at the time of the outburst (JD 2,445,348.0). For the metal abundance we adopt $Z = 0.02$, which also includes carbon, nitrogen, oxygen, and neon with solar composition ratios.

Three different sets of abundance determinations for the ejecta of GQ Mus are available from the literature, but their values are rather scattered, as it appears from Table 1. We here consider three cases, in order of decreasing hydrogen content in the envelope, not directly corresponding to the three sets of abundance determination in Table 1: a) $X = 0.55$, $X_{\text{CNO}} = 0.20$, $X_{\text{Ne}} = 0.0$, and $Z = 0.02$; b) $X = 0.45$, $X_{\text{CNO}} = 0.35$, $X_{\text{Ne}} = 0.0$, and $Z = 0.02$; c) $X = 0.35$, $X_{\text{CNO}} = 0.30$, $X_{\text{Ne}} = 0.0$, and $Z = 0.02$. These composition sets correspond to assuming 25%, 55%, and 100% mixing of C+O WD matter with a hydrogen-rich envelope with solar composition. If we change X_{CNO} while keeping the hydrogen content X constant, the light curves hardly change provided $X_{\text{CNO}} \gtrsim 0.2$.

We have searched for the best fit model by changing the WD mass in steps of $0.05 M_{\odot}$ for the above three sets of chemical compositions.

5. LIGHT CURVE FITTING

We apply to GQ Muscae 1983 the model light curves of classical novae described in the previous section, and evaluate its fundamental parameters. The optical V magnitude and the near infrared I , J , H , and K magnitudes are calculated from free-free emission, while the UV 1455 Å and supersoft X-ray fluxes are obtained from blackbody emission, as illustrated in Figure 5.

Models and observations are compared in Figures 6 – 8 which refer to, respectively, the three following chemical composition sets: $(X, Y, X_{\text{CNO}}, Z) = (0.55, 0.23, 0.20, 0.02)$, $(0.45, 0.18, 0.35, 0.02)$, and $(0.35, 0.33, 0.30, 0.02)$. The white dwarf mass range explored is $M_{\text{WD}} = 0.60$ to $0.80 M_{\odot}$, in $0.05 M_{\odot}$ steps. In each figure, the thick solid line represents the white dwarf mass value that leads to the best representation of the data for the above chemical composition sets.

5.1. Supersoft X-ray fluxes

The decay time of the supersoft X-ray flux is a good indicator of the WD mass (Paper I). Through a careful visual inspection to the data, we have selected the models that best fitted the *ROSAT* observations (Ögelman et al. 1993; Shanley et al. 1995; Orío et al. 2001; Balman & Krautter 2001). The model and the observed supersoft X-ray light curves are reported in Figures 6 – 8.

5.2. Continuum UV 1455 Å fluxes

The light curves in the UV 1455 Å continuum are a good indicator of photospheric temperature during the early decay phase of novae. Such curves are in general quite smooth, as shown by Cassatella et al. (2002) for several objects observed with *IUE*. A comparison of models with observed UV light curves (see Figs. 6 – 8) shows that this is also the case of GQ Mus, except for the two earliest observations on day 37 and 49, and that of day 151. Leaving these data apart, we find that the model that best fits the data is that of a white dwarf with mass $M_{\text{WD}} = 0.75$, 0.7 , and $0.65 M_{\odot}$, for the three above chemical composition sets, respectively. As for the observation of day 151, the large deviation from the model's smooth trend is clearly due to the occurrence of the UV flash discussed in §3.2. The otherwise good agreement between models and observations shown in the above figures may suggest that also the observations of day 37 and 49 are due to a UV flash (see discussion in §6.6).

5.3. Optical and infrared fluxes

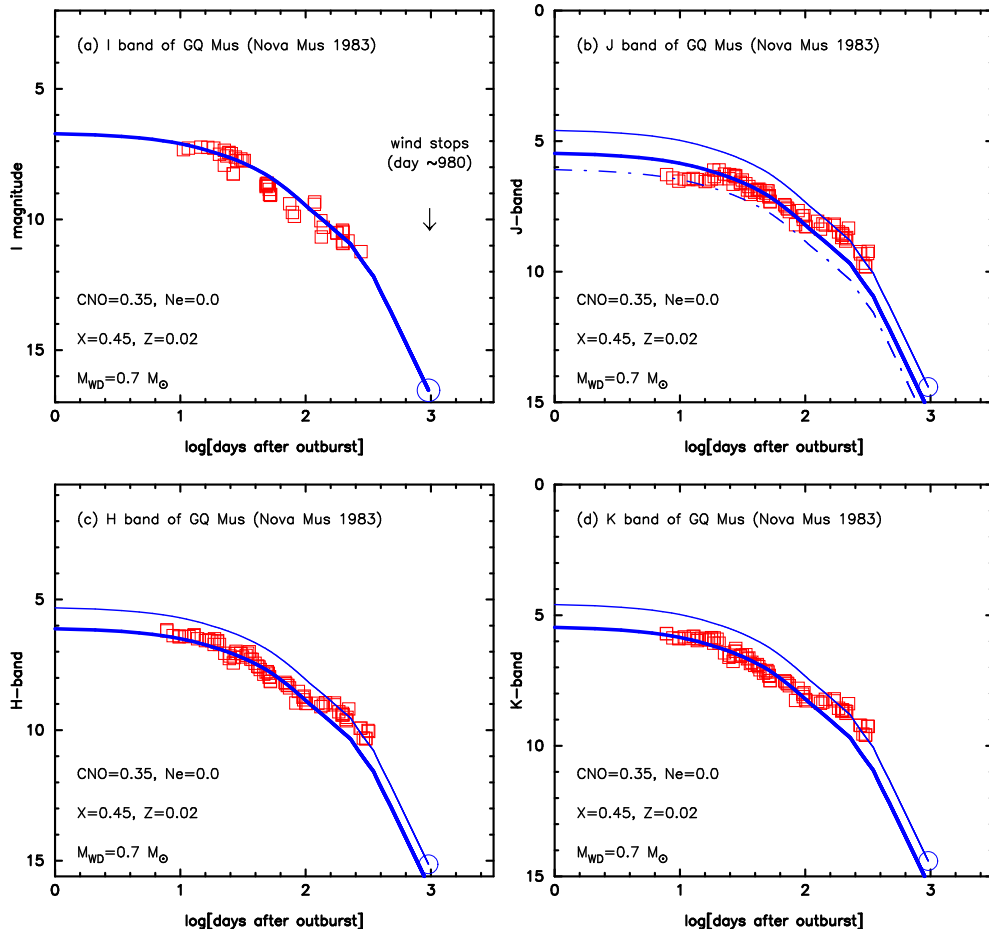


FIG. 9.— Near-infrared multiwavelength light curves (I , J , H , and K) for free-free emission, based on equation (2), and our model light curve corresponding to $M_{\text{WD}} = 0.70 M_{\odot}$, $X = 0.45$, and $X_{\text{CNO}} = 0.35$, together with the observations. *Thick solid line*: fit of the early phase. *Thin solid line*: fit of the late phase after the transition phase (see, e.g., Papers I and II). *Open circles*: end of the wind phase. (a) I magnitudes from free-free emission: These thick and thin lines are overlapped. (b) J magnitudes of free-free emission. The He I $\lambda 10830$ contributes to the J band from the very early phase of the outburst (Whitelock et al. 1984; Krautter et al. 1984), so one more line (*dash-dotted*) is added to represent the very early phase. (c) H magnitudes of free-free emission. (d) K magnitudes of free-free emission. Observational data (I , J , H , and K) are taken from Whitelock et al. (1984) and Krautter et al. (1984). Essentially the same figures are obtained for the other two cases of $M_{\text{WD}} = 0.75 M_{\odot}$, $X = 0.55$, $X_{\text{CNO}} = 0.20$ (see Fig. 6), and $M_{\text{WD}} = 0.65 M_{\odot}$, $X = 0.35$, and $X_{\text{CNO}} = 0.30$ (see Fig. 8).

The visual light curves computed from free-free emission are compared with the observed ones in Figures 6 – 8 for the above chemical composition sets. As discussed in §1 and in Papers I and II, visual magnitudes are contaminated by strong emission lines which will eventually dominate over the continuum, causing an increasing deviation from our free-free models. In GQ Mus, the forbidden [O III] $\lambda\lambda$ 4959, 5007 emission lines already appeared 39 days after the outburst (Krautter et al. 1984). At about this date the observed visual light curve did actually start to show an increasing deviation from the free-free emission model until, by about day 500, the contribution from the emission lines stabilized so that the observed light curve recovered the shape of the model curve. This effect is approximately taken into account by lifting up the template light-curve of GQ Mus by about 4.5 mag, as shown in Figures 6 – 8.

On the other hand, the near infrared $IJKH$ bands are not so heavily contaminated by emission lines, as shown in Figure 9, where the $IJKH$ photometric data from Whitelock et al. (1984) are compared with our theoretical light curve. The figure shows that the model fits the observations reasonably well until about day 100 (thick solid line in the figure), being anyhow the deviations after that date sensibly smaller than in the visual. The contribution from emission lines is particu-

larly small in the I , H , and K bands, whereas the emission line of He I $\lambda 10830$ contributes somewhat to the J band from the very early phase (Whitelock et al. 1984; Krautter et al. 1984). To mimic the different contribution by the emission lines at different phases of the nova development, it is sufficient to lift up the template free-free line two times (starting from the dash-dotted line representing the very early phases, to the thick solid line representing the intermediate phases, and then finally to the thin solid line, representing the late phases).

To summarize the results in this section, the white dwarf mass that best reproduces the X-ray, UV, optical, and near IR is $M_{\text{WD}} = 0.7 \pm 0.05 M_{\odot}$, where the error bar reflects mainly the uncertainty on chemical composition.

6. DISCUSSION

6.1. Overall Development of the Nova Outburst

In this subsection, we analyze the overall development of the nova outburst based on our model of $M_{\text{WD}} = 0.7 M_{\odot}$, $X = 0.45$, $X_{\text{CNO}} = 0.35$, and $Z = 0.02$ (Fig. 7). Figures 10 – 12 report some relevant model predictions and observations as a function of time. First we point out two important epochs of the nova development: one is the end of optically thick wind phase on day 1000, and the other is the end of hydrogen shell

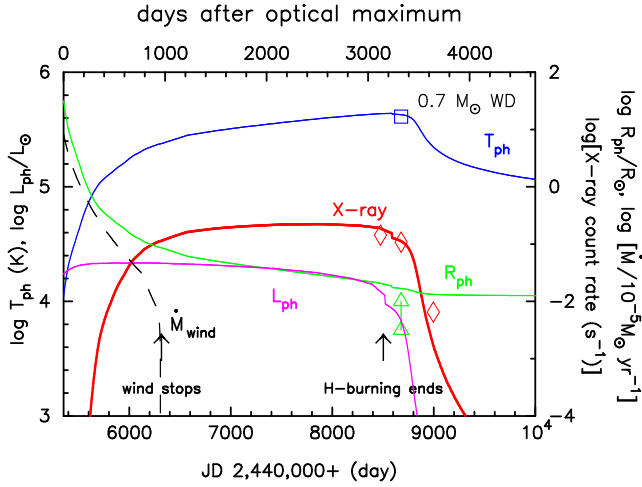


FIG. 10.— Evolution of wind mass loss rate (\dot{M}_{wind} : dashed line), photospheric temperature (T_{ph} : upper thin solid line), photospheric radius (R_{ph} : middle thin solid line), photospheric luminosity (L_{ph} : lower thin solid line), and X-ray flux (thick solid line) of our $M_{\text{WD}} = 0.7 M_{\odot}$ model for the envelope chemical composition of $X = 0.45$, $X_{\text{CNO}} = 0.35$, and $Z = 0.02$. Open diamonds: Observational X-ray count rates taken from Shanley et al. (1995) and Orio et al. (2001). Open squares and open triangles: photospheric temperatures and photospheric radii, respectively, taken from Balman & Krautter (2001).

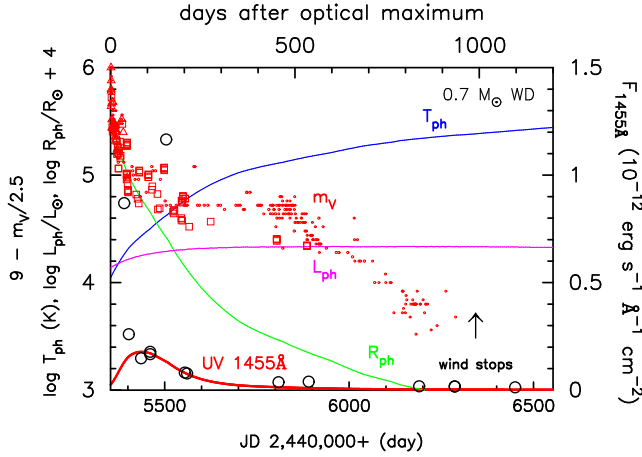


FIG. 11.— Photospheric temperature (T_{ph} : upper thin solid line), photospheric luminosity (L_{ph} : middle thin solid line), photospheric radius (R_{ph} : thin solid line from left-upper to right-lower), and UV 1455 Å flux (thick solid line) of our $M_{\text{WD}} = 0.7 M_{\odot}$ model for the envelope chemical composition of $X = 0.45$ and $X_{\text{CNO}} = 0.35$. Open circles: UV 1455 Å fluxes. Visual magnitude are also shown (as $9 - m_V/2.5$) using the same symbols as in Figs. 6–8.

burning on day 3300 as summarized in Table 3. Because of the rapid shrinking of the photospheric radius (R_{ph}), also the photospheric temperature (T_{ph}) rapidly increases until the wind stops, as indicated in Figure 10. Also the wind mass loss rate (\dot{M}_{wind}) decreases rapidly from $\sim 2 \times 10^{-4} M_{\odot} \text{ yr}^{-1}$ to $1 \times 10^{-7} M_{\odot} \text{ yr}^{-1}$ during the first 1000 days. Thus the total mass ejected by the winds amounts to $\sim 2 \times 10^{-5} M_{\odot}$. After the wind stops, the photospheric radius becomes smaller than $\sim 0.1 R_{\odot}$, and the photospheric temperature eventually becomes larger than 20 eV, so that the nova enters a supersoft X-ray phase. After the hydrogen shell burning ends, the nova cools down rapidly, and a fast decay phase of the supersoft X-ray flux follows, as already shown in the previous section. In what follows, we summarize some relevant observational aspects

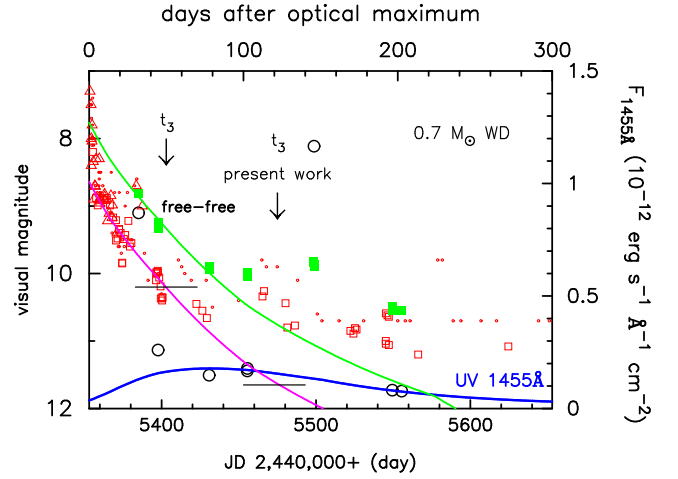


FIG. 12.— Visual and V magnitudes during 300 days after the optical maximum. The same symbols as in Figs. 6–8 except the IUE V_{FES} magnitude (filled squares). Two free-free light curves are plotted both for the IUE V_{FES} magnitudes and for Whitelock et al.'s (1984) V magnitudes. The V_{FES} data are 0.5–0.8 mag brighter than those of Whitelock et al.'s. The t_3 time (left arrow) is estimated to be 50 days from Whitelock et al.'s V magnitudes together with the peak brightness of 7.2 mag (Liller & Overbeek 1983). Note that the decay time (right arrow: $t_3 = 122$ days) corresponding to our universal decline law (lower solid free-free line) is sensibly larger than that previously quoted. See text for more details.

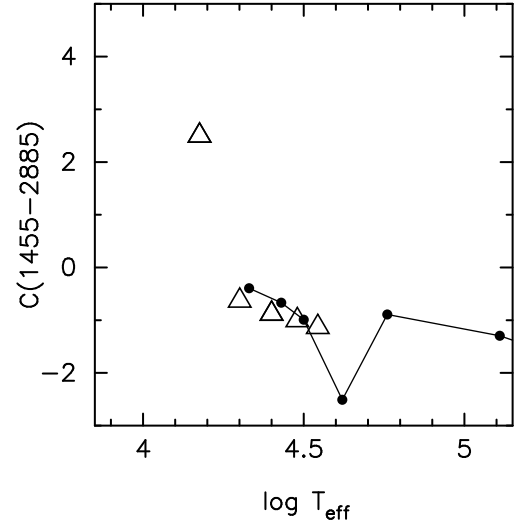


FIG. 13.— Color-temperature relation for nova wind solutions. The UV color of $C(1455-2885)$ is defined by $-2.5 \log(F(1455)/F(2885))$. Filled circles connected with a solid line: reddening-corrected $C(1455-2885)$ v.s. the photospheric temperature T_{eff} corresponding to our best fit model. Open triangles: color-temperature relations estimated from Fig. 10 of Hauschildt et al. (1997) and Fig. 8 of Short et al. (1999). See text for more details.

and make a comparison with our model predictions.

From the coronal lines in the optical spectrum Diaz et al. (1992) deduced a luminosity of $10^{37} - 10^{38}$ ergs s $^{-1}$ and a temperature of $(2-3) \times 10^5$ K. These values are consistent with our model of a $0.7 M_{\odot}$ WD, which provides $T_{\text{ph}} = 4 \times 10^5$ K and $L_{\text{ph}} = 6 \times 10^{37}$ ergs s $^{-1}$ about 2700 days after the outburst, as it may be appreciated from Figure 10.

Diaz et al. (1995) estimated a central source temperature of 164,000 K, a luminosity of $350 L_{\odot}$, and an ejecta mass of $5 \times 10^{-4} M_{\odot}$, about 4000 days after the outburst. For our best-fit model of a $0.7 M_{\odot}$ white dwarf with an initial envelope mass of $\Delta M_0 = 2.7 \times 10^{-5} M_{\odot}$, the total mass lost by the op-

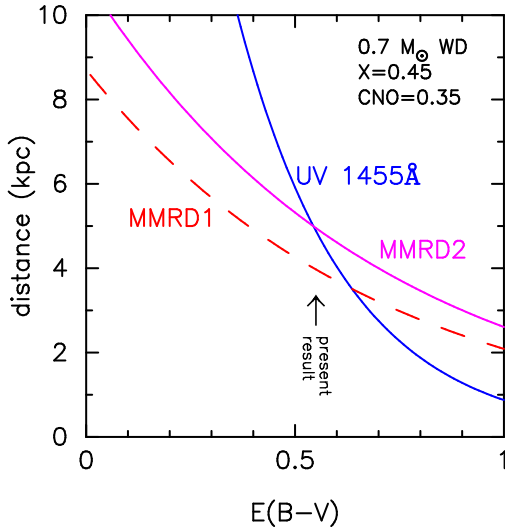


FIG. 14.— Distance-reddening relations derived from the UV 1455 Å fitting (solid line labeled “UV 1455 Å”) of our model $M_{\text{WD}} = 0.7 M_{\odot}$, $X = 0.45$, and $X_{\text{CNO}} = 0.35$ and the maximum magnitude vs. rate of decline (labeled “MMRD1” and “MMRD2”). The dashed line labeled “MMRD1” is a MMRD relation calculated from Schmidt-Kaler’s law, i.e., eq. (5) together with $t_3 = 50$ days. The solid line labeled “MMRD2” is the same MMRD relation calculated from $t_3 = 122$ days estimated from our universal decline law. An arrow indicates our value of $E(B-V) = 0.55$, which is an error-weighted mean of $E(B-V) = 0.51 \pm 0.06$ and 0.58 ± 0.04 in §3.1. See text for more details.

tically thick wind is $\Delta M_{\text{wind}} = 1.9 \times 10^{-5} M_{\odot}$. We also obtain $T_{\text{ph}} = 1.5 \times 10^5$ K and $L_{\text{ph}} = 4 \times 10^{35} \text{ ergs s}^{-1} \approx 100 L_{\odot}$, 4000 days after the outburst, as shown in Figure 10. Our values are then very consistent with those obtained by Diaz et al. (1995), except for their larger ejected mass (see below for another estimate).

The envelope mass itself depends mainly on the white dwarf mass and slightly on the chemical composition. For a $0.65 M_{\odot}$ white dwarf, $X = 0.35$, and $X_{\text{CNO}} = 0.30$, we obtain a slightly larger envelope mass, $\Delta M_0 = 3.6 \times 10^{-5} M_{\odot}$, and a larger wind mass loss, $\Delta M_{\text{wind}} = 2.3 \times 10^{-5} M_{\odot}$. On the other hand, for a $0.75 M_{\odot}$ white dwarf with $X = 0.55$, and $X_{\text{CNO}} = 0.20$, we obtain a slightly smaller envelope mass, $\Delta M_0 = 2.6 \times 10^{-5} M_{\odot}$, and a smaller wind mass loss, $\Delta M_{\text{wind}} = 1.7 \times 10^{-5} M_{\odot}$.

Using their photoionization model, Morisset & Péquignot (1996b) estimated the temperatures during the static phase and at the hydrogen burning turnoff to be 2.5×10^5 K and 4.1×10^5 K, respectively, and an ejected shell mass of $8 \times 10^{-5} M_{\odot}$. These values are consistent with our model, i.e., $> 2.4 \times 10^5$ K, $> 4.4 \times 10^5$ K, and $2 \times 10^{-5} M_{\odot}$. The above authors determined the duration of the wind phase and of the static hydrogen burning phase to be < 0.52 yr and 8.8 yr, to be compared with our values of 2.7 yr and 6.3 yr, respectively. The much longer duration of the wind phase obtained by us is likely due to the rapid decrease of the wind mass loss rate with an e-folding time of 0.24 yr, corresponding to a decrease by a factor of 10 in 0.7 yr.

6.2. Photospheric Temperature Development

Figure 13 shows the reddening corrected UV color index $C(1455-2885)$ as a function of the photospheric temperature obtained from our best-fit model at the time of the individual observations (filled circles). The figure indicates that the color index decreases smoothly with increasing temperature except

for its abrupt decrease at the time of the UV flash on day 151 (note that the temperature increases with time in these early phases).

It is interesting to compare the color- T_{ph} values reported in Figure 13 with those derived from Hauschildt et al. (1997) and Short et al. (1999), who calculated early-time nova spectra using non-LTE atmosphere codes with winds having density and velocity laws within the nova envelope. For this comparison, we have taken the values of $C(1455-2885)$ from Figure 10 of Hauschildt et al. (1997) for $T_{\text{eff}} = 15,000, 20,000, 25,000,$ and $30,000$ K, and from Figure 8 of Short et al. (1999) for $T_{\text{eff}} = 35,000$ K. The model values of $C(1455-2885)$ so obtained are plotted as a function of the corresponding effective temperature in Figure 13 (open triangles). It clearly appears from Figure 13 that the two sets of values are very consistent with each other, except for the UV flash on day 151. This result supports our assumption that the UV 1455 Å flux is reasonably well accounted for by blackbody emission. Indeed, line blanketing is rather small at this wavelength, so that the blackbody model does not deviate much from Hauschildt et al.’s non-LTE models, as already discussed in Paper I.

6.3. Emergence of the secondary component

The mass of the donor star (the secondary component) can be estimated from the orbital period. Diaz & Steiner (1989, 1994) obtained $P_{\text{orb}} = 0.05936$ days (1.425 hr) from the orbital modulations with an amplitude of 0.6 mag. Using Warner’s (1995) empirical formula

$$\frac{M_2}{M_{\odot}} \approx 0.065 \left(\frac{P_{\text{orb}}}{\text{hours}} \right)^{5/4}, \text{ for } 1.3 < \frac{P_{\text{orb}}}{\text{hours}} < 9 \quad (4)$$

we get $M_2 = 0.10 M_{\odot}$. The orbital separation is then $a = 0.59 R_{\odot}$ for $M_{\text{WD}} = 0.7 M_{\odot}$, the effective radius of the Roche lobe for the primary component (white dwarf) is $R_1^* = 0.33 R_{\odot}$, and the effective radius of the secondary is $R_2^* = 0.14 R_{\odot}$. In our model, the companion emerges from the white dwarf envelope when the photospheric radius of the white dwarf shrinks to $R_{\text{ph}} \sim 0.6 R_{\odot}$ (the separation) or $0.3 R_{\odot}$ (the Roche lobe). This happens on about day 330 or 500, respectively, in our best-fit model with $M_{\text{WD}} = 0.7 M_{\odot}$, as shown in Figures 10 and 11.

According to Whitelock et al. (1984), strong infrared coronal lines appeared 57 days after optical maximum in V1500 Cyg, but were not present in GQ Mus as late as 97 days after maximum. Their appearance roughly coincides with the emergence of the companion from the white dwarf photosphere: this suggests that these strong coronal lines arise from the shock between the white dwarf wind and companion star. Indeed, the emergence of the companion in V1500 Cyg took place about 50 days after optical maximum (Paper I), which is consistent with the appearance of the line 57 days after maximum. In the case of GQ Mus, the absence of strong coronal lines on day 97 days is consistent with our model in which the companion emerged about 330 or 500 days after maximum.

In their study of GQ Mus, Krautter & Williams (1989) reported that the [Fe X] $\lambda 6374$ coronal line first appeared 2.2 to 3.4 yrs after the outburst, and became the strongest about 4 years after it. They argued that the coronal line was due to photoionization from a hot radiation source rather than to collisional excitation. In our $0.7 M_{\odot}$ white dwarf model, the optically thick wind stopped about 960 days (2.7 yrs) after the outburst and then the photospheric temperature gradually in-

creased to above 20–25 eV 4 yrs after the outburst, as shown in Figures 10 and 11. These authors suggested that $\sim 3 \times 10^5$ K in 1984, which is consistent with our photospheric temperature of $T_{\text{ph}} = 2.2 \times 10^5$ K 2.2 yr after the outburst (Figs. 10 and 11).

6.4. Hard X-ray component

Ögelman et al. (1987) reported that the count rate of the *EXOSAT* low-energy telescope was about 3×10^{-3} c s $^{-1}$ 400 days to 700 days after optical maximum, a value that gradually decreased to 1×10^{-3} c s $^{-1}$ about 900 days after it.

If the X-rays originates from the shock between the wind and the companion star, the soft X-ray behavior is consistent with our $0.7 M_{\odot}$ white dwarf model (as well as $0.75 M_{\odot}$ and $0.65 M_{\odot}$ white dwarf models), because the emergence of the companion star is predicted to happen on day 330, and the wind stopped at 960 days after optical maximum.

6.5. Distance

Whitelock et al. (1984) and Krautter et al. (1984) have estimated the distance to GQ Mus from the apparent and the absolute V magnitudes at maximum, m_V and M_V . This latter was computed from the t_3 time through the Schmidt–Kaler Maximum Magnitude Rate of Decline (MMRD) relation (Schmidt 1957):

$$M_V = -11.75 + 2.5 \log t_3. \quad (5)$$

Despite the sensibly different input values adopted of 48 and 40 days for t_3 , 0.4 and 0.45 for $E(B-V)$, and 7.2 and 6 for m_V , these authors obtained quite similar values for the distance, 5 kpc and 4.8 kpc, respectively.

A re-analysis of the merged visual magnitude data present in the literature (see plot in Fig. 12) confirms $t_3 \approx 50$ days, in close agreement with Whitelock et al. (1984), so that $M_V = -7.5$ [cf. equation (5)]. If, together with Whitelock et al. (1984), we take $m_{V,\text{max}} = 7.2$ as the best estimate of the apparent magnitude at optical maximum (Liller & Overbeek 1983), we finally obtain the following relation between distance and $E(B-V)$:

$$m_V - M_V = -5 + 5 \log d + 3.1E(B-V) = 14.7, \quad (6)$$

which is labeled “MMRD1” in Figure 14. In particular, the value $E(B-V) = 0.55 \pm 0.05$ obtained in §3.1, corresponds to a distance of $d = 4.0 \pm 0.3$ kpc.

Following the same procedure outlined in Paper I and Kato & Hachisu (2005, 2007), an independent estimate of the distance to GQ Mus can be obtained by comparing the observed light curve in the 1455 Å continuum with the corresponding model fluxes in Figures 6–8, 11, and 12. The calculated flux at $\lambda = 1455$ Å at a distance of 10 kpc for our adopted model ($0.7 M_{\odot}$, $X = 0.45$, $X_{\text{CNO}} = 0.35$) is $F_{\lambda}^{\text{mod}} = 2.85 \times 10^{-12}$ ergs cm $^{-2}$ s $^{-1}$ Å $^{-1}$ on JD 2,445,455.6. The observed flux at the same date is $F_{\lambda}^{\text{obs}} = 1.78 \times 10^{-13}$ ergs cm $^{-2}$ s $^{-1}$ Å $^{-1}$. From these values one obtains the following relation between distance and reddening:

$$m_{\lambda}^{\text{obs}} - M_{\lambda}^{\text{mod}} = 5 \log\left(\frac{d}{10 \text{ kpc}}\right) + A_{\lambda}E(B-V) = 3.01, \quad (7)$$

where $m_{\lambda} = -2.5 \log(F_{\lambda})$, and $A_{\lambda} = 8.3$ (Seaton 1979). This curve, labeled “UV 1455 Å,” is reported in Figure 14. In particular, equation (7) provides a distance of 4.9 ± 0.9 kpc for

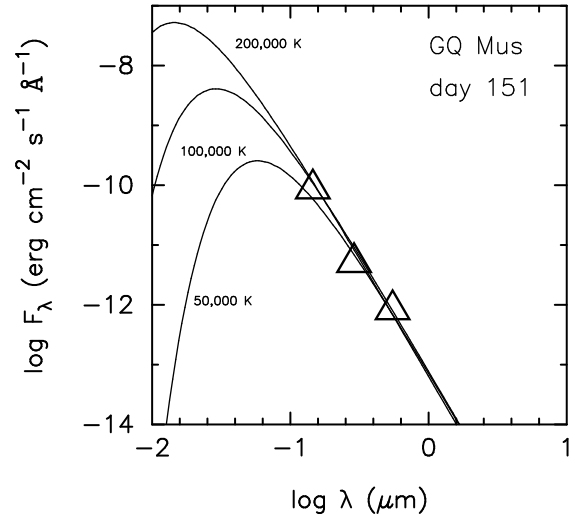


FIG. 15.— Energy distribution for three bands of UV 1455 Å, 2885 Å, and IUE FES visual (open triangles) on day 151. Blackbody energy distributions are also plotted for three temperatures of 50,000, 100,000, and 200,000 K.

$E(B-V) = 0.55 \pm 0.05$, which is sensibly larger than that obtained from MMRD1.

An alternative way to determine the distance of GQ Mus is to compare the shape of the theoretical visual light curve (based on the free-free model) with the observed visual fluxes. Such a comparison, done in Figure 7 is very instructive because it shows that the object was up to 1.5 magnitudes brighter than predicted by our universal light curve model during the earliest phases (until day 10). It is then legitimate to consider GQ Mus as a super-bright nova. An extreme case of this type was V1500 Cyg, which, near peak luminosity was about 4 magnitudes brighter than the Eddington limit for a $1.0 M_{\odot}$ white dwarf (Ferland et al. 1986). It is interesting to note that if such a super-bright phase is ignored in GQ Mus, the t_3 and t_2 times of the theoretical light curve that best fits the observations are considerably longer than the observation indicates at face value: we in fact estimate $t_3 = 122$ days and $t_2 = 67$ days. From equation (5) we then obtain $M_{\text{ff,max}} = -6.53$ at the time of maximum light ($t = 8$ days). Since the apparent magnitude at visual maximum of our theoretical light curve is $m_{\text{ff,max}} = 8.66$ mag (see Fig. 7), the distance to GQ Mus can be estimated to be 5.0 ± 0.3 kpc for $E(B-V) = 0.55 \pm 0.05$. If the reddening is not fixed, the following relation applies:

$$m_{\text{ff,max}} - M_{\text{ff,max}} = -5 + 5 \log d + 3.1E(B-V) = 15.19, \quad (8)$$

which is plotted in Figure 14 (labeled “MMRD2”). The two curves UV 1455 Å and MMRD1 cross at $d = 3.5$ kpc and $E(B-V) = 0.64$, whereas the curves UV 1455 Å and MMRD2 cross at $d = 5.1$ kpc and $E(B-V) = 0.54$, as it appears from Figure 14. Since $E(B-V) = 0.55$ is the weighted mean of the reddening determinations done in §3.1, we take this value together with $d = 5$ kpc as the best estimates compatible with the observations. The errors on the reddening and the distance are ≈ 0.05 dex and ≈ 0.5 kpc, respectively.

6.6. The UV flashes

Here we estimate the total luminosity of the UV flash on day 151 and discuss its outburst nature. From Figure 2, we have obtained the excess of energy above the smooth decline for each of the three bands, i.e., 1455 Å, 2885 Å, and V_{FES} , which are plotted in Figure 15. These fluxes are consistent with the energy distribution from a blackbody with a

TABLE 2
PROPERTIES OF GQ MUSCAE

subject	...	data	units	reference
discovery	...	2,445,352.6	JD	Liller & Overbeek (1983)
nova speed class	...	moderately fast		Whitelock et al. (1984)
t_2	...	18	days	Whitelock et al. (1984)
t_3	...	48	days	Whitelock et al. (1984)
$M_{V,\text{peak}}$ from t_3	...	-7.55	mag	Whitelock et al. (1984)
distance from t_3	...	5	kpc	Whitelock et al. (1984)
dust	...	no		Whitelock et al. (1984)
orbital period	...	1.425	hr	Diaz et al. (1995)
$E(B-V)$...	4.5		Krautter et al. (1984)
wind phase	...	< 0.5	yr	Morisset & Péquignot (1996b)
H-burning phase	...	3300	days	The first observation of <i>IUE</i> on day 37 also shows a high UV flux compared with our white dwarf model. A close look at the optical brightness in Figure 12 indicates a small peak around day 37. This event may also be due to another mass ejection episode. Note that these mass ejection episodes add to the major underlying continuous mass ejection process from the optically thick wind, which endures until day ~ 1000 , as shown in Figure 10.

TABLE 3
SUMMARY OF OUR MODEL

subject	...	data	units
outburst day	...	2,445,348.0	JD
opt. maximum	...	2,445,352.6	JD
t_2	...	67 ^a	days
t_3	...	122 ^a	days
$M_{V,\text{peak}}$ from t_3	...	-6.53 ^b	mag
distance from t_3	...	5.0 ± 0.3	kpc
secondary mass	...	0.1 ^c	M_\odot
$E(B-V)$...	0.55 ± 0.05	
distance by UV fit	...	4.9 ± 0.9	kpc
t_{break}^d	...	275	day
WD mass	...	0.7 ± 0.05	M_\odot
WD envelope mass	...	$(2.6-3.6) \times 10^{-5}$	M_\odot
mass lost by wind	...	$(1.7-2.3) \times 10^{-5}$	M_\odot
wind phase	...	1000	days
H-burning phase	...	3300	days
separation	...	0.6	R_\odot
companion's emergence	...	330 ± 30	days
UV flash luminosity	...	$\gtrsim 45,000^e$	L_\odot

^a t_2 and t_3 are calculated from our fitted universal decline law.

^b calculated from equation (5) together with t_3 above.

^c estimated from equation (4).

^d see Paper I.

^e estimated from a blackbody of $T \sim 10^5$ K.

temperature of $\gtrsim 100,000$ K. Hassall et al. (1990) also estimated the temperature from a Zanstra-like method, based on the He II/H β ratio, to be 85,000 to 100,000 K. The photospheric temperature of our $0.7 M_\odot$ white dwarf model are about 30,000 K (on day 108) before the UV flash and about 60,000 K (on day 202) after the UV flash.

Assuming blackbody emission, we can estimate the size of the emitting region from $(R/d)^2 \approx 10^{-21}$ for $T = 100,000$ K. Taking $d = 5$ kpc, the radius of the emission region is $R \sim 7 R_\odot$. The total flux is estimated to be 1.7×10^{38} erg s⁻¹ ($\approx 45,000 L_\odot$) from $L = 4\pi R^2 \sigma T^4$. On day 151, the photospheric radius of our $0.7 M_\odot$ white dwarf model is as small as $1.3 R_\odot$ and the photospheric temperature is as low as 42,000 K. Therefore, the estimated radius and blackbody temperature, $R \sim 7 R_\odot$ and $T \gtrsim 100,000$ K, suggest an episodic expansion and strong heating of the photosphere. This was probably due to a dynamical mass ejection episode and to strong shock heating. The UV flash is anyhow a short-lived event that hardly contributes to the total ejecta mass, as suggested by the fast recovery of the emission line spectrum by day 202 and by the negligible effect on the optical light curves.

7. CONCLUSIONS

We have applied the ‘‘universal decline law’’ of classical novae described in §4 to GQ Muscae 1983 and derived various parameters of the nova. Our main results may be summarized as follows:

1. We show that the ‘‘universal decline law’’ reproduces well the observed light curves of GQ Mus in the optical and in the near infrared *I*, *J*, *H*, and *K* bands.

2. Our blackbody light curve model for the UV 1455 Å band can reproduce the observed UV 1455 Å fluxes except two UV flashes on day 37 and 151.

3. The UV flash on day 151 described in §3.2 was accompanied by a mass ejection episode seen as a fast wind with a terminal velocity of about 3200 km s⁻¹.

4. An analysis of the *IUE* reprocessed data of GQ Mus indicates $E(B-V) = 0.55 \pm 0.05$, a value that is larger than previously reported.

5. We find that the mass of the WD component of GQ Mus is $0.7 \pm 0.05 M_\odot$ for the adopted envelope chemical composition of $X = 0.35-0.55$, $X_{\text{CNO}} = 0.2-0.35$. This value has been derived by comparing predicted fluxes from our models with the observations in the supersoft X-ray, in the UV, and in the optical and near infrared, obtained at different times.

6. We have estimated a mass of $\Delta M_{\text{wind}} \sim 2 \times 10^{-5} M_\odot$ lost by the wind.

7. We have estimated a distance of $d \sim 5$ kpc.

We thank Albert Jones (RASNZ) for providing us with their machine readable visual estimates of GQ Mus 1983 and also AAVSO for the visual data of GQ Mus 1983. We are also grateful to the anonymous referee for useful comments that helped to improve the paper. This research has been supported in part by the Grant-in-Aid for Scientific Research (16540211, 16540219, 20540227) of the Japan Society for the Promotion of Science and by INAF PRIN 2007.

APPENDIX

COLOR OF FREE-FREE LIGHT CURVES OF NOVAE

In this and previous papers we have modeled the time evolution of novae in the continuum and compared the results with observed light curves. Such a study is hampered by the presence of emission lines, which give rise to sensible distortions in most

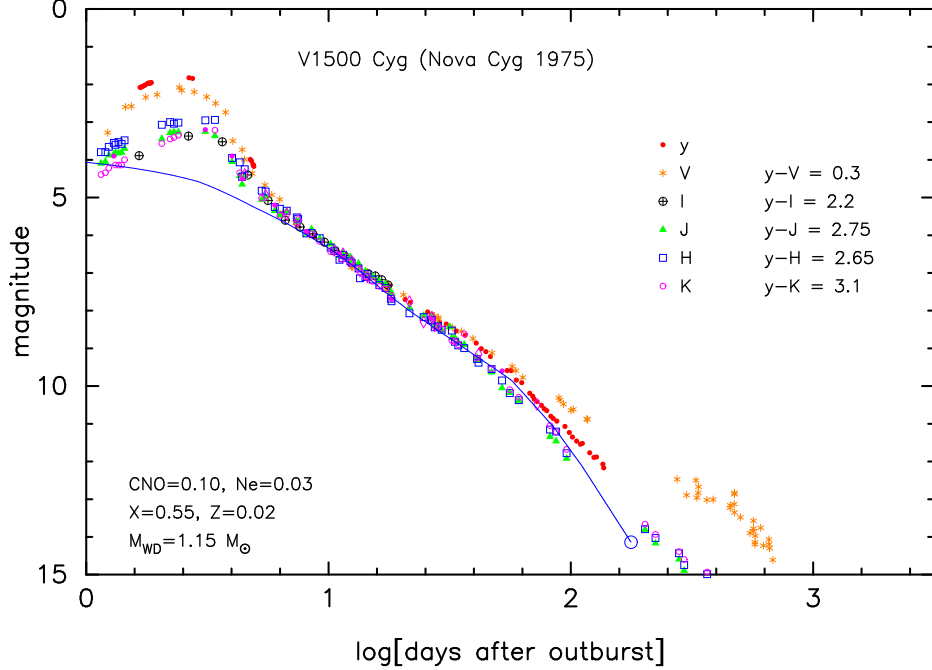


FIG. 16.— Observed y , V , I , J , H , and K light curves for the classical nova V1500 Cyg. Each light curve is shifted down to the y light curve by $\Delta m_\lambda = \Delta V = y-V = 0.3$, $\Delta I = y-I = 2.2$, $\Delta J = y-J = 2.75$, $\Delta H = y-H = 2.65$, and $\Delta K = y-K = 3.1$. These light curves are well overlapped between day 6 and 30 (days after outburst). Filled circles: y magnitudes. Asterisks: V magnitudes. Plusing open circles: I magnitudes. Filled triangles: J magnitudes. Open squares: H magnitudes. Open circles: K magnitudes. Solid line with a large open circle: our model light curve for the $1.15 M_\odot$ WD with $X = 0.55$, $X_{\text{CNO}} = 0.10$, $X_{\text{Ne}} = 0.03$, and $Z = 0.02$ (see Paper I). The large open circle at the right-lower edge of the line indicates the end of optically thick wind phase.

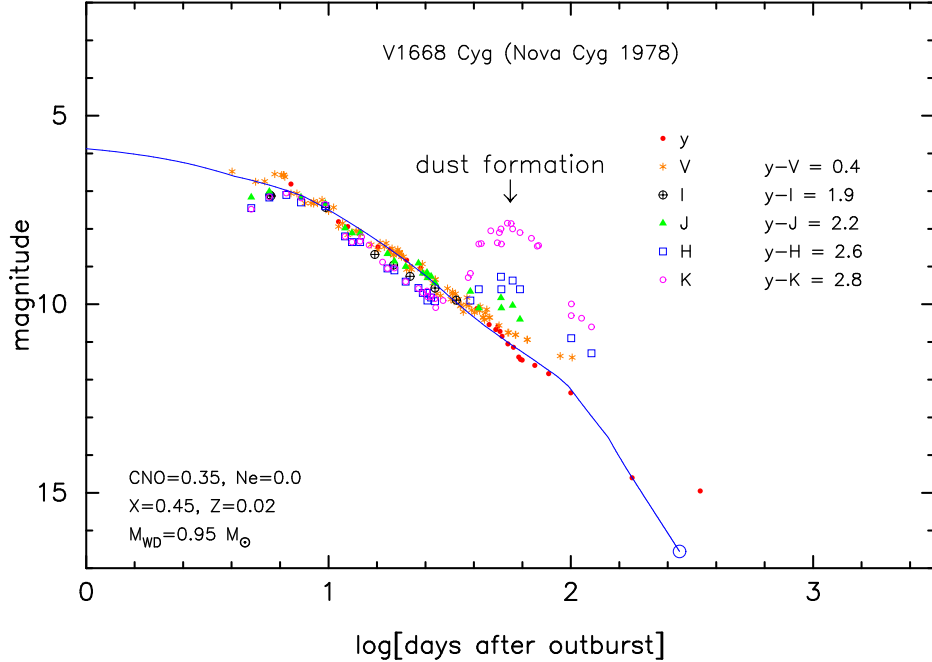


FIG. 17.— Same as Fig.16 but for the classical nova V1668 Cyg. Each light curve is overlapped with the y light curve between day 6 and 30. Optically thin dust was formed around day 35–50. Solid line with a large open circle: our model light curve for the $0.95 M_\odot$ WD with $X = 0.45$, $X_{\text{CNO}} = 0.35$, and $Z = 0.02$ (see Paper I).

photometric bands (see §1), especially at some nova phases. To evaluate the contamination by emission lines, we take advantage of the fact that the intrinsic colors of free-free emission are constant with time because of $\lambda F_\lambda \propto \lambda^{-1}$ for free-free emission. Here, we consider four classical novae that are well observed in various photometric bands: V1500 Cyg, V1668 Cyg, V1974 Cyg, and GQ Mus.

Intrinsic $V-R$, $V-I$, $V-J$, $V-H$, and $V-K$ colors from free-free emission, as calculated from $\lambda F_\lambda \propto \lambda^{-1}$, are reported in the second column of Table 4. If reddening is known, observed colors are obtained from

$$m_V - m_\lambda = (M_V - M_\lambda)_0 + c_\lambda E(B-V), \quad (\text{A1})$$

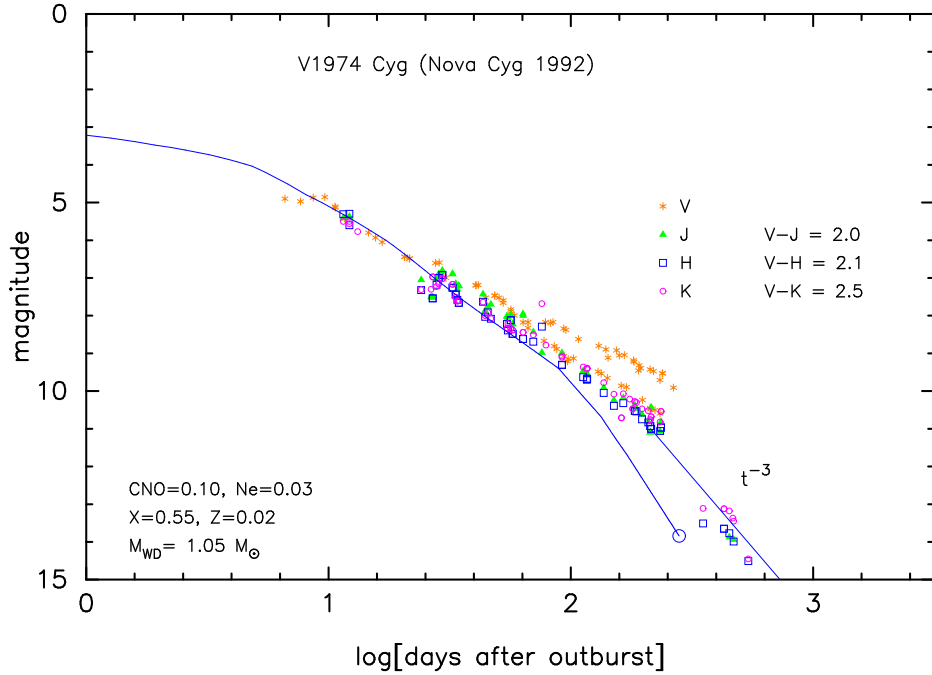


FIG. 18.— Same as Fig.16 but for the classical nova V1974 Cyg. No y and I magnitudes are available for this nova, so that we show only three colors of $V-J$, $V-H$, and $V-K$. Each light curve is overlapped with the V light curve during day 10–30. Solid line with a large open circle: our model light curve for the $1.05 M_{\odot}$ WD with $X = 0.55$, $X_{\text{CNO}} = 0.10$, $X_{\text{Ne}} = 0.03$, and $Z = 0.02$ (see Paper I). Solid line with t^{-3} : a decline law of $F_{\lambda} \propto t^{-3}$ (see eq.[3]).

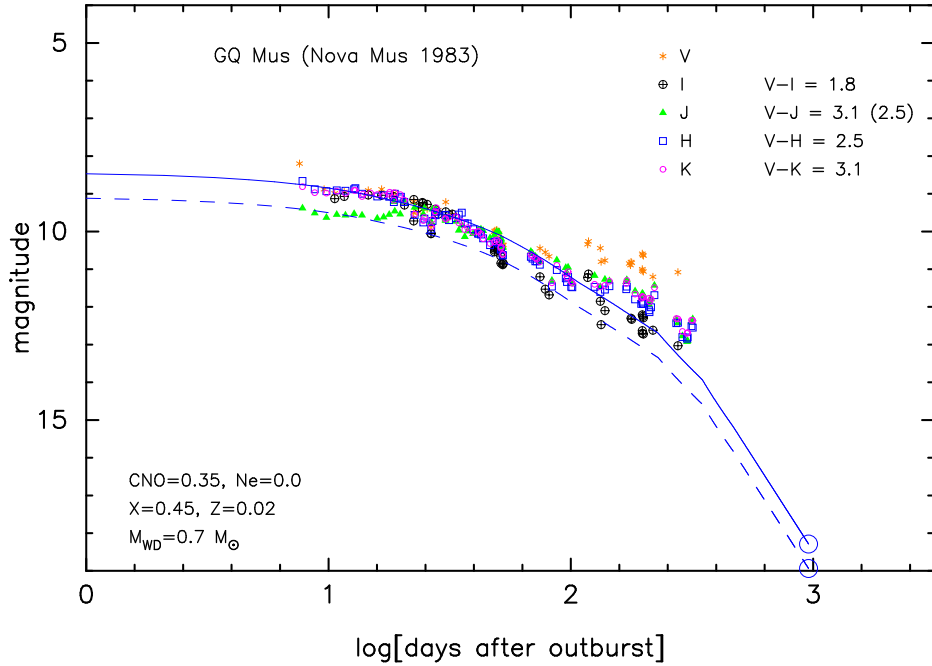


FIG. 19.— Same as Fig.16 but for the classical nova GQ Mus. No y magnitudes are available for this nova, so that we show four colors of $V-I$, $V-J$, $V-H$, and $V-K$. Each light curve is overlapped with the V light curve during day 8–50 except for the J magnitudes. The J magnitudes are fitted only during day 20–100. As mentioned in §5.3, the J magnitude brightened up by 0.6 mag after day 15. If we overlap the J light curve between day 8 and 15, the color decreases from $V-J = 3.1$ to $V-J = 2.5$ as shown in the figure. Solid line with a large open circle: our model light curve for the $0.7 M_{\odot}$ WD with $X = 0.45$, $X_{\text{CNO}} = 0.35$, and $Z = 0.02$ (see §5). Dashed line with a large open circle: same as that for the solid line but vertically shift down by 0.6 mag to match the J magnitudes during day 8–15.

where $(M_V - M_{\lambda})_0$ is the intrinsic color and c_{λ} is the reddening coefficient listed in the second and third columns of Table 4, respectively.

In the following subsection, we will compare the observed colors with those calculated from equation (A1) for classical novae V1500 Cyg, V1668 Cyg, V1974 Cyg, and GQ Mus. Figures 16–19 demonstrate that the shape of light curves is almost independent of the wavelength, which is a characteristic feature of free-free emission (see equation [2]). In these figures, we shift each observed light curve down by Δm_{λ} and overlap it on the observed y (or V) light curve. Then, we obtain the color of

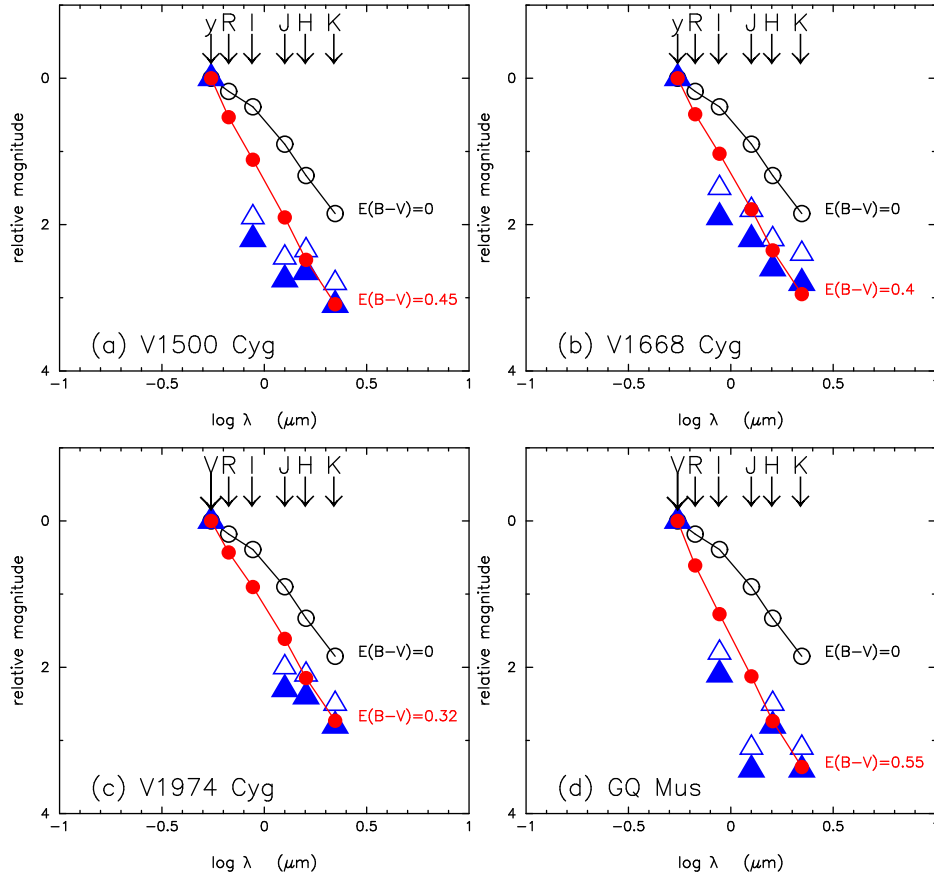


FIG. 20.— The $V-R$, $V-I$, $V-J$, $V-H$, and $V-K$ (open triangles) and the $y-R$, $y-I$, $y-J$, $y-H$, and $y-K$ (filled triangles) for the four classical novae: (a) V1500 Cyg, (b) V1668 Cyg, (c) V1974 Cyg, and (d) GQ Mus. Open and filled circles represent, respectively, the intrinsic and the reddening corrected colors as expected from free-free emission (see Table 4). See equation (A1) for the relation between free-free color and reddening). Note that the H and K band is the least contaminated by emission lines, so that the $y-H$ and $y-K$ colors are in a reasonable agreement with the theoretical values. See text for more details.

TABLE 4
COLORS OF FREE-FREE LIGHT CURVES

color ^a ($m_V - m_\lambda$)	...	intrinsic ($(M_V - M_\lambda)_0$)	coefficient (c_λ)
$V-V$...	0	0
$V-R$...	0.18	0.7812
$V-I$...	0.39	1.6058
$V-J$...	0.90	2.2258
$V-H$...	1.33	2.5575
$V-K$...	1.85	2.7528

^a color is calculated from $(m_V - m_\lambda) = (M_V - M_\lambda)_0 + c_\lambda E(B-V)$, where $(M_V - M_\lambda)_0$ is the intrinsic color of the free-free spectrum and c_λ is the reddening coefficient

$\Delta m_\lambda = m_y - m_\lambda$ (or $\Delta m_\lambda = m_V - m_\lambda$) from the definition of $m_\lambda + \Delta m_\lambda = m_y$ (or $m_\lambda + \Delta m_\lambda = m_V$). The colors thus obtained are listed in each figure and plotted in Figure 20.

V1500 Cyg

For V1500 Cyg, we use the y photometry in Lockwood & Millis (1976) and the V data in Tempest (1979), I data in Thé & van der Klis (1976). The J , H , and K observations were taken from Ennis et al. (1977), Kawara et al. (1976), and Gallagher & Ney (1976). These light curves are plotted in Figure 16 with each light curve being overlapped on the y magnitude. The spectrum became that for free-free emission about 4–5 days after the outburst while it was that for blackbody during the first 3 days (Gallagher & Ney 1976). So, we shift each observed light curve down by Δm_λ and overlap it on the observed y light curve between day 6 and 30. Then, we obtain the color of $\Delta m_\lambda = m_y - m_\lambda$ as listed in Figure 16.

The intrinsic color indices, $(M_V - M_\lambda)_0$, for $V-R$, $V-I$, $V-J$, $V-H$, and $V-K$ of free-free emission (Table 4) are plotted in Figure 20a (open circles) together with $E(B-V) = 0.45$ (filled circles) calculated from equation (A1).

The $V-I$, $V-J$, $V-H$, and $V-K$ color indices obtained from Figure 16 are plotted in Figure 20a (open triangles). If strong

emission lines are present in the spectrum, observed colors deviate from those calculated from equation (A1). In fact, the V band is not emission-line free, being contaminated by strong emission lines even between day 6 and 30. The amount of contamination can be estimated from $y-V = 0.3$ because the y band is almost emission-line free. This value tells us that strong emission lines contribute about 30% of the energy flux to the V band. The $y-I$, $y-J$, $y-H$, and $y-K$ color indices are also plotted in Figure 20a (filled triangles).

A somewhat larger contamination is present in the I and J bands while the H and K bands are not so heavily contaminated by emission lines. For V1500 Cyg, the $y-H$ and $y-K$ colors are in a reasonable agreement with equation (A1) with $E(B-V) = 0.45$.

V1668 Cyg

Figure 17 shows y , V , I , J , H , and K light curves of V1668 Cyg. Here the y magnitude observations are taken from Gallagher et al. (1980), the V data are from Mallama & Skillman (1979) and Duerbeck et al. (1980), the I magnitudes from Deroux (1978), and the J , H , and K magnitudes from Gehrz et al. (1980). Each light curve is shifted down to overlap with the y light curve between day 6 and 30 because the spectrum was no longer that for free-free emission after day 35 due to dust formation. The colors are summarized in this figure and are also plotted in Figure 20b. The I band is strongly, the J band is slightly, while the H and K bands are not heavily contaminated by emission lines. For V1668 Cyg, the $y-H$ and $y-K$ color are in reasonable agreement with equation (A1) together with $E(B-V) = 0.40$ (Stickland et al. 1981). Note also that the V band is contaminated by emission lines as suggested from $y-V = 0.4$.

V1974 Cyg

For V1974 Cyg, no y and I photometry is available. Figure 20c shows the $V-J$, $V-H$, and $V-K$ colors obtained from Figure 18, where V magnitudes are taken from Chochol et al. (1993) and the J , H , and K magnitudes are from Woodward et al. (1997). Open triangles denote the observed colors, which follow quite well the calculated ones with $E(B-V) = 0.32$ (Chochol et al. 1993). However, the V band is contaminated by emission lines even at early phases as already shown in V1500 Cyg and V1668 Cyg. If we subtract this contribution of $\Delta V \sim 0.3$ (estimated from the spectrum in Fig. 2 of Barger et al. 1993), i.e., $y-V = 0.3$, we obtain the corrected colors (filled triangles) as shown in Figure 20c. The J band is heavily contaminated by O I, Paschen β , and γ , while the H and K bands are not so heavily contaminated (Woodward et al. 1997). This explains why the $y-H$ and $y-K$ colors, corrected by $\Delta V = y-V = 0.3$, are in good agreement with the expected values from free-free emission.

GQ Mus

In Figure 20d we plot (as open triangles) the observed $V-I$, $V-J$, $V-H$, and $V-K$ colors from Figures 19, and compare them with the intrinsic colors from free-free emission calculated from equation (A1) for $E(B-V) = 0.55$ (filled circles). The observed colors are in reasonably good agreement with the calculated ones.

However, the V band is not emission-line free, being contaminated by strong emission lines even in the early phase (e.g., $\sim 30\%$ from Fig. 2 of Whitelock et al. 1984). This contributes $\Delta V = y-V \sim 0.3$ to the colors, so we subtract this from the original value of V , and obtain the corrected colors of $y-I$, $y-J$, $y-H$, and $y-K$ (filled triangles) as shown in Figure 20d. The I band is strongly contaminated by O I line and the J band is also very strongly contributed by Paschen β line (e.g., Fig. 3 of Whitelock et al. 1984). Consequently, both the $y-I$ and $y-J$ colors (corrected by $\Delta V = y-V = 0.3$) are 0.8 and 1.3 mag below the calculated ones, respectively. On the other hand, the H and K bands are not heavily contaminated by strong emission lines (e.g., Fig. 3 of Whitelock et al. 1984). This explains why both the $y-H$ and $y-K$ colors corrected by $\Delta V = y-V = 0.3$ are in good agreement with equation (A1) of $E(B-V) = 0.55$.

REFERENCES

- Andrae, J., & Drechsel, H. 1990, *Physics of Classical Novae*, eds. A. Cassatella and R. Viotti (Berlin: Springer-Verlag), 204
- Balman, Ş., & Krautter, J. 2001, MNRAS, 326, 1441
- Balman, Ş., Krautter, J., & Ögelman, H. 1998, ApJ, 499, 395
- Barger, A. J., Gallagher, J. S., Bjorkman, K. S., Johansen, K. A., & Nordsieck, K. H. 1993, ApJ, 419, L85
- Bateson, F. M. 1998, Inf. Bul. Variable Stars, 2316, 1
- Cassatella, A., Altamore, A., & González-Riestra, R. 2002, A&A, 384, 1023
- Cassatella, A., Lamers, H. J. G. L. M., Rossi, C., Altamore, A., González-Riestra, R. 2004, A&A, 420, 571
- Cassatella, A., Altamore, A., González-Riestra, R. 2005, A&A, 439, 205
- Chochol, D., Hric, L., Urban, Z., Komzik, R., Grygar, J., & Papousek, J. 1993, A&A, 277, 103
- de Freitas Pacheco, J. A., & Codina, S. J. 1985, MNRAS, 214, 481
- Deroux, J. K. 1978, Inf. Bul. Var. Stars, 1519, 1.
- Diaz, M. P., & Steiner, J. E. 1989, ApJ, 339, L41
- Diaz, M. P., & Steiner, J. E. 1994, ApJ, 425, 252
- Diaz, M. P., Williams, R. E., Phillips, M. M., & Hamuy, M. 1995, MNRAS, 277, 959
- Diaz, M. P., Williams, R. E., Phillips, M. M., & Steiner, J. E. 1992, Cataclysmic Variable Stars, ed. N. Vogt, (ASP Conf. Ser. 29), 362.
- Dinerstein, H. L. 1986, AJ, 92, 1381
- Duerbeck, H. W., Rindermann, R., & Seitter, W. C. 1980, A&A, 81, 157
- Ennis, D., Beckwith, S., Gatley, I., Matthews, K., Becklin, E. E., Elias, J., Neugebauer, G., & Willner, S. P. 1977, ApJ, 214, 478
- Ferland, G. J., Lambert, D. L., & Woodman, J. H. 1986, ApJS, 60, 375
- Gallagher, J. S., & Ney, E. P. 1976, ApJ, 204, L35
- Gallagher, J. S., Kaler, J. B., Olson, E. C., Hartkopf, W. I., & Hunter, D. A. 1980, PASP, 92, 46
- Gehrz, R. D., Hackwell, J. A., Grasdalen, G. I., Ney, E. P., Neugebauer, G., & Sellgren, K. 1980, ApJ, 239, 570
- Grevesse, N., & Anders, E. 1989, Cosmic Abundances of Matter, ed. C. J. Waddington (New York: AIP), 1
- Groenewegen, M. A. T., & Lamers, H. J. G. L. M. 1989, A&AS, 79, 359
- Hachisu, I., & Kato, M. 2001a, ApJ, 553, L161
- Hachisu, I., & Kato, M. 2001b, ApJ, 558, 323
- Hachisu, I., & Kato, M. 2004, ApJ, 612, L57
- Hachisu, I., & Kato, M. 2006, ApJS, 167, 59 (Paper I)
- Hachisu, I., & Kato, M. 2007, ApJ, 662, 552 (Paper II)
- Hachisu, I., Kato, M., Kato, T., & Matsumoto, K. 2000, ApJ, 528, L97
- Hachisu, I., Kato, M., & Nomoto, K. 1996, ApJ, 470, L97
- Hachisu, I., Kato, M., & Nomoto, K. 1999a, ApJ, 522, 487
- Hachisu, I., Kato, M., Nomoto, K., & Umeda, H. 1999b, ApJ, 519, 314
- Hachisu, I., Kato, M., & Schaefer, B. E. 2003, ApJ, 584, 1008
- Hassall, B. J. M., et al. 1990, *Physics of Classical Novae*, eds. A. Cassatella and R. Viotti (Berlin: Springer-Verlag), 202

- Hauschildt, P. H., Shore, S. N., Schwarz, G. J., Baron, E., Starrfield, S., & Allard, F. 1997, *ApJ*, 490, 803
- Hummer, D. G., & Storey, P. J. 1987, *MNRAS*, 224, 801
- Iglesias, C. A., & Rogers, F. J. 1996, *ApJ*, 464, 943
- Kaler, J. B. 1986, *PASP*, 98, 243
- Kato, M. 1983, *PASJ*, 35, 507
- Kato, M. 1997, *ApJS*, 113, 121
- Kato, M. 1999, *PASJ*, 51, 525
- Kato, M., & Hachisu, I., 1994, *ApJ*, 437, 802
- Kato, M., & Hachisu, I., 2005, *ApJ*, 633, L117
- Kato, M., & Hachisu, I., 2007, *ApJ*, 657, 1004
- Kawara, K., Maihara, T., Noguchi, K., Oda, N., Sato, S., Oishi, M., & Iijima, T. 1976, *PASJ*, 28, no. 1, 1976, p. 163
- Krautter, J., Beuermann, K., Leitherer, C., Oliva, E., Moorwood, A. F. M., Deul, E., Wargau, W., Klare, G., Kohoutek, L., van Paradijs, J., & Wolf, B. 1984, *A&A*, 37, 307
- Krautter, J., & Williams, R. 1989, *ApJ*, 341, 968
- Lamers, H. J. G. L. M.; Cerruti-Sola, M.; Perinotto, M. 1987, *ApJ*, 314, 726
- Liller, W., & Overbeek, M. D. 1983, *IAU Circ.*,
- Livio, M. 1992, *ApJ*, 393, 516
- Lockwood, G. W., & Millis, R. L. 1976, *PASP*, 88, 235
- Mallama, A. D., & Skillman, D. R. 1979, *PASP*, 91, 99
- McLaughlin, D. B. 1942, *ApJ*, 95, 428
- Morisset, C., & Péquignot, D. 1996a, *A&A*, 312, 135
- Morisset, C., & Péquignot, D. 1996b, *A&A*, 313, 611
- Ögelman, H., Krautter, J., & Beuermann, K. 1987, *A&A*, 177, 110
- Ögelman, H., Orio, M., Krautter, J., & Starrfield, S. 1993, *Nature*, 361, 331
- Orio, M., Covington, J., Ögelman, H. 2001, *A&A*, 373, 542
- Payne-Gaposchkin, C. 1957, *The Galactic Novae* (Amsterdam: North-Holland)
- Péquignot, D., Petitjean, P., Boisson, C., & Krautter, J. 1993, 271, 219
- Rosenbush, A. E. 1999a, *Astrophysics*, 42, 43
- Rosenbush, A. E. 1999b, *Astrophysics*, 42, 140
- Schmidt, Th. 1957, *Z. Astrophys.*, 41, 181
- Seaton, M. J. 1979, *MNRAS*, 187, 73
- Shanley, L., Ögelman, H., Gallagher, J. S., Orio, M., & Krautter, J. 1995, *ApJ*, 438, L95
- Short, C. I., Hauschildt, P. H., & Baron, E. 1999, *ApJ*, 525, 375
- Stickland, D. J., Penn, C. J., Seaton, M. A., Snijders, M. A., J., Storey, P. J. 1981, *MNRAS*, 197, 107
- Tempest, P. 1979, *Astron. Nachrichten*, Bd. 300, 51
- Thé, P. S., & van der Klis, M. 1976, *Inf. Bul. Var. Stars*, 1089, 1.
- Vorontsov-Velyaminov, B. A. 1948, *Gaseous nebula and novae*, Moscow-Leningrad, Izd. Akad. Nauka (in Russian)
- Warner, B. 1995, *Cataclysmic variable stars*, Cambridge, Cambridge University Press
- Whitelock, P. A., Carter, B. S., Feast, M. W., Glass, I. S., Laney, D., Menzies, J. W., Walsh, J., & Williams, P. M. 1984, *MNRAS*, 211, 421
- Woodward, C. E., Gehrz, R. D., Jones, T. J., Lawrence, G. F., & Skrutskie, M. F. 1997, *ApJ*, 477, 817